**FINAL REPORT
CONTRACT NAS8-39238**

A DIAGNOSTIC SYSTEM FOR STUDYING ENERGY PARTITIONING AND ASSESSING THE RESPONSE OF THE IONOSPHERE DURING HAARP MODIFICATION EXPERIMENTS

Frank T. Djuth
John H. Elder
Kenneth L. Williams

Geospace Research, Inc.
550 N. Continental Boulevard, Suite 110
El Segundo, CA 90245

**Report Date
15 May 1996**

**Period of Performance
30 September 1991 through 31 December 1993**

TABLE OF CONTENTS

1. Overview of Research Program

The work performed under this contract focused on the construction of several key radio wave diagnostics in support of the HF Active Auroral Ionospheric Research Program (HAARP). The HAARP facility is classically referred to as an HF ionospheric modification facility. HF ionospheric modification entails the use of high-power, high-frequency (~2-15 MHz) radio waves to modify the earth's ionosphere. This generally involves the utilization of large ground-based facilities capable of transmitting ~0.5 to >1 MW of HF power continuously. (A limited number of facilities capable of pulsed operations only are located in the former Soviet Union.) The one-way antenna gain tends to be in the range of 17 to 23 dBi. Experimental results presented below were acquired at two such facilities: one located at Arecibo, Puerto Rico, the other at Tromsø, Norway. The frequency of the high-power waves is typically adjusted so that radio wave reflection occurs in the ionospheric region under study. Waves having either O-mode or X-mode polarization are normally transmitted. For most of the observations described in this report, O-mode polarization waves were used to modify the ionospheric F region (between 200 and 350 km altitude). The F-region modification process entails a variety of effects including the heating of the ambient electron gas, changes in bulk electron density, the formation of ionospheric irregularities, the excitation of Langmuir turbulence, and the acceleration of background thermal electrons to suprathermal energies. Competition among these various phenomena determine the partitioning of HF energy in the plasma. The overall goal of this program is to obtain a detailed understanding of the partitioning process.

This research program led to the design, development, and fabrication of a variety of hardware units and to the development of several menu-driven software packages for data acquisition and analysis. The principal instrumentation includes one HF (28 MHz) radar system (transmitter/receiver), one VHF (50 MHz) radar system (transmitter plus a center line and frequency agile receiver), and a high-speed radar processor consisting of three separable processing units. The processor system supports the HF and VHF radars and is capable of acquiring very detailed data with large incoherent scatter radars. In addition, a tunable HF receiver system having high dynamic range was developed principally for measurements of stimulated electromagnetic emissions (SEE) [e.g., *Thidé et al.*, 1995]. The HF receiver is capable of measuring weak broadband (100 kHz) SEE emissions emanating from the modified ionospheric volume and can be used to examine the phase/amplitude of the ionospherically-reflected pump wave. It is also effective in investigations of artificial periodic irregularities in the ionosphere [*Fejer et al.*, 1984].

The diagnostic systems described above are specifically designed to address questions related to the partitioning of HF energy in the auroral ionosphere and to provide a sensitive measure of the response of the F-region and E-region ionospheres to HAARP energy deposition.

In establishing equipment/radar processor requirements, Geospace Research, Inc. relied heavily on its past experimental experience with the HF modification facility at Arecibo, Puerto Rico, and the 1.2 GW effective radiated power facility near Tromsø, Norway. The various diagnostic systems provide a potent means both for studying HAARP ionospheric modifications and for identifying how certain types of modifications can be controlled, mitigated, or altered. Recent results in the field of ionospheric modification physics tend to confirm this conclusion [Djuth, 1993].

The HF and VHF radars are optimized for measurements of short-scale geomagnetic field-aligned irregularities excited by the high-power HF beam. The high-speed radar processor can be used with the HAARP incoherent scatter radar to yield high-resolution data needed to chart the development of HF-induced Langmuir and ion-wave turbulence in the ionosphere. Moreover, this same processor can be used to make high-resolution observations of temperature and electron density perturbations created by HAARP. Finally, the sensitive HF receiver provides a way of determining the time scale and magnitude of energy deposition in the ionosphere, furnishes information about bulk changes in electron density and large-scale vertical ionospheric motion, and serves as an effective diagnostic for estimating the total amount of Langmuir turbulence excited in the modified volume.

A variety of laboratory and field tests were performed with the HAARP equipment. Laboratory tests included the use of test signals to assess the performance of the four receivers, the processing of ionosphere modification data stored on wideband analog tape to test the radar processor units [Djuth et al., 1994a; Djuth et al., 1996a], and tests of the HF/VHF transmitters at low power. All diagnostic support equipment was extensively tested in the laboratory environment to verify the compliance with manufacturer specifications. In addition, the radars, processors, HF receiver, and most of the support equipment were tested in demanding field experiments.

The HAARP equipment was used to support VHF and incoherent scatter observations made during the Combined Release and Radiation Effects Satellite (CRRES) El Coqui rocket campaign in Puerto Rico (May - July, 1992) [Djuth et al., 1995; Bernhardt et al., 1995]. This represented an important test of processor system speed and performance in a critical measurement program. Other tests were performed in conjunction with an Arecibo ionospheric modification campaign (July 1992) and in incoherent scatter radar studies of photoelectron-enhanced plasma lines [Djuth et al., 1994b; Djuth et al., 1996b]. The HF receiver was first employed in an ionospheric modification experiment conducted at the High-Power Auroral Stimulation (HIPAS) Observatory located near Fairbanks, Alaska (October, 1992). This was an attempt to use partial reflections from pulses transmitted from HIPAS to determine the D-region electron density profile.

The HAARP equipment proved versatile enough to serve as dual-use diagnostics in two military programs and two new scientific initiatives. In particular, the 50 MHz radar, the standard radar processor system, and the processor system developed for the HF receiver were all used to support a theater ballistic missile observation program. Experiments focusing on Lance missile plume scatter were conducted at White Sands Missile Range from March through June, 1993 [see e.g., *Djuth et al.*, 1996a]. This was followed by a series of VHF, UHF, and S-band radar experiments from NASA/Wallops Island Flight Facility in 1994 and 1995. In this case, the focus was on plumes from Sergeant launch vehicles. These observations made use of the HAARP 50 MHz radar and all of the standard radar processor units (which were attached to all radar systems). In September/October 1994 the HAARP 28 MHz radar was deployed in Chile for equatorial irregularity studies, and in summer 1995 the HAARP 50 MHz radar was used to search for flashes above thunderstorm clouds (so-called sprites and blue jets). This was followed by a highly successful HIPAS experiment (October 1995), which entailed the detection of HF-induced artificial periodic irregularities in the *D*-region [*Djuth et al.*, 1996c]. In these experiments the HF receiver was used along with one of the standard radar processor units. Finally, the HAARP 28 MHz radar is scheduled for a sprite/blue jet campaign in the midwest (summer, 1996), and it is anticipated that the HAARP 50 MHz radar will be deployed in the Caribbean for Arecibo HF modification experiments (August, 1996). In general, experience has shown that the HAARP diagnostics are powerful tools for studying diverse ionospheric modification phenomena and that they are flexible enough to support a host of unanticipated missions beyond the scope of HAARP.

2. Principal Diagnostic Instrumentation Constructed for HAARP

The principal instrumentation developed for the HAARP project consists of a 28-MHz radar system, a 50 MHz radar system, an HF receiver system, standard data acquisition systems for the VHF radars and for incoherent scatter radars, and a data acquisition unit for measurements of stimulated electromagnetic emissions with the HF receiver. Key system specifications for these units are provided in Table 1 below.

Table 1. HAARP Diagnostic Specifications

28-MHz RADAR SYSTEM

Frequency Range: 27 - 29 MHz

Peak Power: 50 kW

Duty Cycle: 2%

Pulse Widths: 2 - 100 μs

Control: Manual or Remote (using built-in microprocessor)

Receiver: Single Channel, Complex Voltage Output

Receiver Dynamic Range: 80 dB

Phase Code: Determined by TTL Input

50-MHz RADAR SYSTEM

Frequency Range: 48 - 52 MHz

Peak Power: 50 kW

Duty Cycle: 2%

Pulse Widths: 1 - 100 μs

Control: Manual or Remote (using built-in microprocessor)

Receiver: Two Channels, Center Line and Plasma line, Complex Voltage Outputs

Receiver Dynamic Range: 80 dB

Phase Code: Determined by TTL Input

HF RECEIVER SYSTEM

Frequency Range: 2 - 12 MHz

Tuning: Direct Digital Synthesis

Receiver: Single Channel, Complex Voltage Output

Receiver Dynamic Range: 80 dB

DATA ACQUISITION SYSTEMS

Incoherent Scatter Radar and VHF radars

Three Phase-Locked Units (can be separately operated)

Records Raw Voltages with Real-Time RTI Displays

Four "Housekeeping" Channels per Unit

Digitization at 8 Bits. Peak: 3 x (6 M Samples (Complex) per sec)

Average: 3 x (670 K bytes per second)

Digitization at 14 Bits. Peak: 3 x (1 M Samples (Complex) per sec)

Average: 3 x (670 K bytes per sec)

IPP Range: 200 μs to >120 ms

SEE Unit for HF Receiver

16-Bit Digitization: 125 K Samples (Complex) Continuous

Wideband Analog Tape Recorder

14 Channels, up to 2 MHz Bandwidth per Channel

Dynamic Range: S/N between 26 dB and 50 dB (depends on bandwidth, record mode)

OTHER INSTRUMENTATION
>   Computer-Controlled Spectrum Analyzer - SEE Measurements
>   Complete Support Instrumentation for Field Campaigns

3. Complete Listing of HAARP Diagnostic Equipment

A comprehensive listing of HAARP diagnostic equipment developed under this contract is presented in Appendix A.

4. User Manuals

Technical details relating to the operation and maintenance of the HAARP diagnostics and related software modules are provided in a series of manuals. These consist of manuals written by Geospace Research, Inc. and standard manufacturer's manuals for support instrumentation such as oscilloscopes, wave form generators and the like. The GRI-supplied manuals are listed below along with a brief description of their contents.

4.1 Specialized Equipment Manuals

The key HAARP diagnostic equipment and associated software were designed and constructed to meet the specific requirements of HF ionospheric modification experiments. Many of the instruments are flexible enough to be used for a variety of scientific and military projects. Portions of the radar hardware were developed by GRI in association with La Salle Research Corporation and Genesis Engineering. All of the radar processing hardware as well as all software modules were developed by GRI.

4.1.1 VHF Pulse Transmitter Manual

This manual describes the parameters, set up, initial turn-on procedures, and remote and local operational procedures for the La Salle Research Corporation 50 (49.92) MHz and 28 (27.90) MHz radar transmitters. The overall system includes a multi-voltage power supply, power amplifier, microcontroller, solid state driver, and the transmit/receive switch. With the exception of the power amplifier stage (resonantly-tuned to either 49.92 MHz or 27.90 MHz) and the tuned transmit/receive switch, both radar transmitters are identical in design. The transmitters drive a 50-ohm load, which may be an antenna system or a test load. Depending on pulse width, the radar transmitter will yield a peak pulse power of 40 - 50 kW. The user should carefully design/construct the transmission lines and the antenna system so that they have the appropriate power handling capability. When the transmitters are used for HF ionospheric modification studies, coaxial, collinear antennas are often used. A detailed description of the design and construction of these antennas is provided in an article by *Balsley and Ecklund* [1972]. The transmitter specifications are provided in Table 2 below.

TABLE 2. VHF TRANSMITTER SPECIFICATIONS

PARAMETER	50 MHz Transmitter	28 MHz Transmitter
Operating Frequency Range	48 MHz - 52 MHz	27 MHz - 29 MHz
Pulse Width		
Minimum	1 microsecond	2 microseconds
Maximum	100 microseconds	100 microseconds
Pulse Rise Time	< 1 microsecond	< 2 microseconds
Pulse Decay Time	< 1 microsecond	< 2 microseconds
Transmit/Receive switching time	≤ 2 microseconds	≤ 4 microseconds
Peak Envelope Power		
Pulse widths: 1 - 5 µs	50 kW	50 kW
Pulse widths: 5 - 100 µs	40 kW	40 kW
Maximum Duty Cycle	2%	2%
Amplification	One solid-state stage Two vacuum-tube stages	One solid-state stage Two vacuum-tube stages
Cooling	Forced-air	Forced-air
Power	220/240 VAC 50/60 Hz	220/240 VAC 50/60 Hz

4.1.2 RX50-1 Receiver Manual

This manual describes the operation of the center line receiver used with the 50 MHz transmitter. This system was built by LaSalle Research Corporation under the direction of GRI. Receiver specifications are presented in Table 3.

4.1.3 RX50-PL Receiver Manual

This manual provides details concerning the operation of the plasma line (PL) receiver built for the 50 MHz transmitter. The PL receiver has similar (in most areas identical) characteristics to those of the RX50-1 system. The only distinguishing feature is its frequency tuning capability. Direct digital synthesis allows the plasma line receiver to tune between 44 and 50 MHz with 1 Hz frequency resolution.

Table 3

La Salle Research Corp. MODEL RX50-1 Specifications

Frequency	Selectable, 49.80 and 49.92 MHz, TCXOs
Input	Designed to Use an External GaAs FET preamp
Output	Quadrature Outputs may be set to +/- 5 Vdc, +/- 10 Vdc, or 0-5 Vdc. Will drive up to 50 ft of 50 ohm coaxial cable
AC Power	Wired for 120 VAC 50/60 Hz but may be configured for 240 VAC operation. 2 amp fuse required.
Size	Rack Mount 5.25" H by 19" W by 17" D
Weight	24 pounds
Control Inputs	TTL compatible, high true
Preamp Power	15 Vdc through 262 ohm 1 W resistor provides 12 Vdc for preamp with short circuit protection. May be switched off.
TX Pulse Output	RF pulse Compatible with LSRC transmitters
Phase Code	TTL high inverts phase of TX pulse
Blanking	TTL high removes LO signal for phase detector
External Oscillator	A 0 dBm external may be used as a LO
Factory Installed Baseband Filters	1.0 MHz and 100 kHz

4.1.4 RX28-1 Receiver Manual

This manual describes the operation of the center line receiver used with the 28 MHz transmitter. This system was built by LaSalle Research Corporation under the direction of GRI. Receiver specifications are presented in Table 4. The 28 MHz radar system does not have a plasma line receiver as in the case of the 50 MHz radar.

4.1.5 RXHF-1 Receiver Manual

This manual furnished the technical details concerning the operation of the HF receiver designed to monitor stimulated electromagnetic emissions from the ionosphere. This system was built by LaSalle Research Corporation under the direction of GRI. Receiver specifications are presented in Table 5.

4.1.6 Radar Interface Box Design Manual

The radar interface box (RIB) manual describes the hardware unit used to synchronize the radar processor to the radar system itself. The RIB allows the radar processors to access the proper signals from the radar and the station. It also generates signals needed during the acquisition of data. It consists of three major assemblies: a control circuit board, a display circuit board, and a buffer circuit board. These boards are contained within the RIB and are connected to the outside world via various cable assemblies.

4.1.7 Interpulse Period Generator

The Interpulse Period Generator (IPG) manual describes the unit which issues logic pulses to the radar transmitter and receiver. The IPG serves as a controller for the VHF (28 MHz and 50 MHz) radar systems. It produces TTL synchronization pulses to mark the beginning of the interpulse period (IPP), and issues the proper TTL pulses to enable the VHF radar transmit/receive (T/R) switch, generate a radio frequency (RF) pulse, and provide a blanking pulse for the radar receiver.

4.1.8 Pseudo-Random Number Phase Shift Generator

This manual discusses the design and operation of the Pseudo-Random Number Phase Shift Generator. This is essentially a TTL random code generator to be used in conjunction with other hardware present at large incoherent scatter radar sites. It is the key component for the implementation of the Coded Long-Pulse radar technique (CLP) on incoherent scatter radars [*Sulzer*, 1986a]. CLP is a very powerful technique that has been applied in the past to studies of Langmuir turbulence excited by high-power radio waves in the ionosphere. Results of CLP studies at Arecibo Observatory are described by *Fejer et al.* [1991]; observations from Tromsø, Norway are presented by *Djuth et al.* [1994a]. More generally, the technique can also be used to investigate a variety of processes in the natural ionosphere *Djuth et al.* [1994b]. The CLP technique allows wideband spectral measurements to be made with very good range resolution. The range resolution is determined by how quickly the phase of the transmitted incoherent radar

Table 4

La Salle Research Corp. MODEL RX28-1 Specifications

Frequency	Selectable, 27.8 and 27.9 MHz, TCXOs
Input	Designed to Use an External GaAs FET preamp
Output	Quadrature Outputs may be set to +/- 5 Vdc, +/- 10 Vdc, or 0-5 Vdc. Will drive up to 50 ft of 50 ohm coaxial cable
AC Power	Wired for 120 VAC 50/60 Hz but may be configured for 240 VAC operation. 2 amp fuse required.
Size	Rack Mount 5.25" H by 19" W by 17" D
Weight	24 pounds
Control Inputs	TTL compatible, high true
Preamp Power	15 Vdc through 262 ohm 1 W resistor provides 12 Vdc for preamp with short circuit protection. May be switched off.
TX Pulse Output	RF pulse Compatible with LSRC transmitters
Phase Code	TTL high inverts phase of TX pulse
Blanking	TTL high removes LO signal for phase detector
External Oscillator	A 0 dBm external may be used as a LO
Factory Installed Baseband Filters	1.0 MHz and 100 kHz

Table 5

La Salle Research Corp. MODEL RXHF-1 Specifications

Frequency	Direct Digital Synthesis -- 2-12 MHz
Input	BNC Antenna Connector
Output	Quadrature Outputs may be set to +/- 5 Vdc, +/- 10 Vdc, or 0-5 Vdc. Will drive up to 50 ft of 50 ohm coaxial cable.
AC Power	Wired for 120 VAC 50/60 Hz but may be configured for 240 VAC operation. 2 amp fuse required.
Size	Rack Mount 5.25" H by 19" W by 17" D
Weight	24 pounds
Reference Oscillator	40 MHz TCXO
External Oscillator	A 0 dBm external oscillator may be used.
Factory Installed Baseband Filters	500 kHz and 100 kHz

signal can be reversed 180°. At Arecibo, the phase reversal rate is 1 MHz; this yields a range resolution of 150 m. At Tromsø, the best phase reversal rate that we have been able to achieve is 2 MHz (75 m range resolution). With the HAARP incoherent scatter radar, a phase reversal rate of 5 MHz (30 m range resolution) is anticipated. We have designed the Pseudo-Random Number Phase Shift Generator to make full use of a system with 5 MHz transmission bandwidth.

The Phase Shift Generator produces a continuous pseudo-random TTL pulse train. At incoherent scatter radar sites, this pulse train is gated by TTL logic used to issue the radio frequency (RF) pulse. The gating logic is usually supplied by the incoherent scatter radar site, but it can also be implemented with an RF switch and a pulse generator. Five pulse generators useful in this regard are supplied as part of the HAARP support diagnostics.

4.2 Software Manuals

The GRI software manuals document both the data-acquisition software and the data analysis software. The principal radar data-taking program is called HiRes and the associated quick-look analysis program is React. Two additional data-acquisition programs are used for stimulated electromagnetic emissions (SEE) observations. Much of the detailed data analysis is performed with MATLAB, a high level computer language. Utilities are supplied by GRI to facilitate the transfer and interpretation of radar data files by MATLAB.

4.2.1 HiRes User's Manual

This manual describes the menu-driven data acquisition program used with the high-speed radar processors. The High Resolution Signal Acquisition System (HiRes) is used for the digitization of an analog signal. Generally, the analog source is a radar receiver channel or an analog tape recording device. The data-acquisition system is designed to acquire massive amounts of data at high sampling speeds. There are three separate acquisition units similar, but not identical, in design. Each unit samples a complex (in-phase, quadrature) voltage output from a radar receiver or a pair of analog tape recorder channels. The pair of complex data channels are simultaneously sampled with 8-bit digitization precision. The system as configured has a peak sampling rate of 6 megasamples (complex) per second and a maximum average throughput rate of between 600 and 700 kbytes per second. With all three units simultaneously operating, the average throughput is ~2 Mbytes per second.

A PC-based architecture is used for the design of the processors. The processor hardware unit consists of a customized PC, a radar interface box (RIB), and peripherals. The peripherals include a 680 MByte external hard disk drive; an external Exabyte 8500 tape drive with a capacity of 5 Gbyte for each 8-mm tape; and an external Bernoulli 90-Mbyte disk drive. The peripherals are connected to the computer with SCSI cables, whereas custom cabling is used for connections involving the RIB.

11

4.2.2 HiRes Data-Acquisition Program, Listing, and Reference Guide

The version of the final delivered code is 1.57. This manual contains programmer's notes and listings of the assembly code, header file formats, and C code. A structure tree and cross reference table is also provided.

4.2.3 ReAct User's Manual

This user's guide provides instructions for a menu-driven program used to obtain a "quick look" at data acquired with the HAARP VHF radars or an incoherent scatter radar. The ReAct Analysis Program provides a means for rapid analysis of HIRES data. Once ReAct has been invoked, the screen displays three windows labeled Time, Program Parameters, and Main Menu. They provide access to the information and functions needed for HIRES data analysis. Analysis beyond that provided by ReAct may readily be performed in the MATLAB (V.3.5) programming environment or with other user-supplied software. ReAct may be used to generate (dump) MATLAB files of HIRES data or the GetHdr.Mx3 and GetRec.Mx3 MATLAB function programs may be used to import HIRES data directly into MATLAB.

4.2.4 ReAct Data-Acquisition Program, Listing, and Reference Guide

The version of the final delivered code is 2.65. This manual contains programmer's notes and listings of the assembly code, header file formats, and C code. A structure tree and cross reference table is also provided.

4.2.5 SEE Data-Acquisition System User's Manual

The Stimulated Electromagnetic Emission (SEE) user's manual provides detailed instructions for the hardware setup and the software programs used by the two PC-based SEE data collection units. The first unit is referred to as the SEE Processor, whereas the second is termed the General Purpose Interface Bus (GPIB) Acquisition Unit. The SEE Processor employs the LaSalle Research Corporation HF receiver as an input. Data is continuously digitized to 16-bit precision with the aid of an Ariel DSP-32C board.

With the GPIB Acquisition Unit, data is collected by connecting an HF antenna directly to the input of the HP 3589A Spectrum/Network Analyzer (50 Ω impedance). Individual SEE spectra are processed with the spectrum analyzer and then transferred to the PC via the National Instruments IEEE interface. The spectrum analyzer is completely controlled by the GPIB Acquisition Unit. A menu-driven program operated from the GPIB PC is used to acquire data. The screen of the spectrum analyzer serves as a real-time display. Data files are continuously transferred from the spectrum analyzer and stored on the PC hard disk until the data-taking program is terminated from the menu.

An effective strategy for acquiring SEE data is to use the GPIB Acquisition Unit as a background monitor to determine whether the desired SEE signals are present. When the proper

conditions occur, high time resolution measurements of SEE can then be made with the 16-bit SEE Processor.

4.2.6 GPIB Data-Acquisition Program for SEE, Listing, and Reference Guide

This program has no version number. The manual contains programmer's notes and listings of the header file formats and C code. A structure tree and cross reference table is also provided. The program preset parameters are described in the manual's Appendix.

4.2.7 16-Bit SEE Data-Acquisition Program, Listing, and Reference Guide

This program has no version number. The manual contains programmer's notes and listings of the 16-bit digital signal processor code, header file formats, and C code. A structure tree and cross reference table is also provided.

4.2.8 GRI MATLAB and DOS Utilities User's Manual

During the course of this research project, GRI generated several MATLAB and DOS utilities that are quite helpful in the analysis of data. This manual documents these software aids. The key programs are GETPSD, GetHDR & GETREC, Rasta, and xREN. The GETPSD.MX3 MEX file is used to access .PSD files from within MATLAB 3.5 without running any translation programs. This function extracts a single spectrum in the form of a real vector from the .PSD files. GETHDR is a function which returns numerous header parameters from data files generated by HIRES. GETREC is a function which returns a selected record from files created by the HIRES program. The Rasta program creates raster displays from MATLAB files. Finally, the utility xREN is used for renaming files so that they have unique file names. For example, a data acquisition program could produce an output file with the name DATA.ACQ. If the program were run again, the first DATA.ACQ would be overwritten. In situations like this, xREN resolves the problem by automatically appending a four digit integer to each data file.

4.2.9 HAARP Processor Software Kit

This deliverable consists of five 3.5-inch floppy diskettes containing both the source code and the executable code for all HAARP software programs. Additional diskettes contain word processor (Microsoft Word) files for five of the HAARP manuals. Finally, the PC boot files are provided on a diskette with an annotated description of the various *.bat and *.sys files.

5. HAARP and HAARP-Related Publications

As noted in Section 1, the HAARP equipment developed under contract NAS8-39238 has been used in a variety of different experiments. The has fostered much spin-off science and has resulted in many publications. A list of HAARP and HAARP-related publications is provided below.

13

Bernhardt, P. A., C. L. Siefring, P. Rodriguez, D. G. Haas, M. M. Baumback, H. A. Romero, D. A. Solin, F. T. Djuth, L. M. Duncan, D. E. Hunton, C. J. Pollock, M. P. Sulzer, C. A. Tepley, L. S. Wagner, and J. A. Goldstein, The ionospheric focused heating experiment, *J. Geosphys. Res.*, *100*, 17331-17345, 1995.

Djuth, F. T., Nonlinear resonance effects produced in the *F* region by high-power radio waves, *The Review of Radio Science 1990-1992*, ed. W. R. Stone, Oxford University Press, Chapter 29, 601-610, 1993.

Djuth, F. T, P. Stubbe, M. P. Sulzer, H. Kohl, M. T. Rietveld, and J. H. Elder, Altitude characteristics of plasma turbulence excited with the Tromsø superheater, *J. Geosphys. Res.*, *99*, 333-339, 1994a.

Djuth, F. T., M. P. Sulzer, and J. H. Elder, Application of the Coded Long Pulse Technique to Plasma Line Studies of the Ionosphere, *Geophys. Res. Lett.*, *21*, 2725-2728, 1994b.

Djuth, F. T., M. P. Sulzer, J. H. Elder, and K. M. Groves, The CRRES AA 2 release: HF wave-plasma interactions in a dense Ba^+ cloud, *J. Geophys. Res.*, *100*, 17347-17366, 1995.

Djuth, F. T., J. H. Elder, and K. L. Williams, Auroral and Midlatitude Radar Studies: Radar Methods for Improved Diagnostics of the HF-modified and Natural Ionospheres, Phillips Laboratory Report PL-TR-96-2070, 66 pp., 1996a.

Djuth, F. T., M. P. Sulzer, and J. H. Elder, Electron density imprints of gravity waves in the lower thermosphere, *J. Geophys. Res.*, in press, 1996b.

Djuth, F. T., M. P. Sulzer, and J. H. Elder, Detection of artificial plasma inhomogeneities in HF modification experiments at HIPAS, *J. Geophys. Res.*, submitted, 1996c.

Djuth, F. T., M. P. Sulzer, and J. H. Elder, Langmuir oscillations and the standing wave pattern at Arecibo, *J. Geophys. Res.*, submitted, 1996.

The above publications describe a variety of the diverse applications of HAARP instrumentation in scientific investigations. The numerous experimental efforts have repeatedly confirmed that the performance of the HAARP diagnostics meet or exceed the specifications summarized above and set forth in detail in the comprehensive set of HAARP manuals. For illustrative purposes, the use of the HAARP radar processor system with the incoherent scatter radar at Arecibo Observatory, Puerto Rico is described below. This example was chosen because the wideband nature of the Arecibo radar challenges the limits of the high-speed radar processors. The scientific investigation is focused on electron density imprints of atmospheric gravity waves in the lower thermosphere between 115 altitude to 165 km. However, measurements have also been made across a much broader altitude region from 105 km to 550 km; these results show that gravity wave imprints can be detected at heights as high as 550 km.

6. An Example of the Use of the HAARP Radar Processors with an Incoherent Scatter Radar: Detection of Electron Density Imprints of Gravity Waves in the Lower Thermosphere

Very accurate measurements of electron density can be made at Arecibo Observatory, Puerto Rico by applying the coded long-pulse (CLP) radar technique [Sulzer, 1986a] to plasma line echoes from daytime photoelectrons [Djuth et al., 1994b]. In the lower thermosphere above Arecibo, background neutral waves couple to the ionospheric plasma, typically yielding ~1-3% electron density "imprints" of the waves. These imprints are present in all observations; they are decisively detected at 30-60 standard deviations above the "noise level" imposed by the measurement technique. Complementary analysis and modeling efforts provide strong evidence that these fluctuations are caused by internal gravity waves. Time series analyses show that fluctuations are abruptly cut off at the Brunt-Väisälä frequency, and phase velocities are always directed downward. Vertical wavelengths are typically observed in the range 5-15 km between 115 and 170 km altitude. Many waves have vertical wavelengths short enough to be quenched by kinematic viscosity. In general, the observed density imprints are relatively "clean" in that their vertical wavelength spectrum is characteristically narrow-banded. This may be symptomatic of wave breaking or other nonlinear processes occurring at mesospheric altitudes.

6.1 Introduction

A variety of aeronomic studies can be performed by applying the coded long-pulse (CLP) radar technique [Sulzer, 1986a] to echoes from photoelectron-enhanced plasma lines (PEPLs) in the daytime ionosphere [e.g., Yngvesson and Perkins, 1968]. Initial results of tests performed with the 430 MHz incoherent scatter radar at Arecibo, Puerto Rico are described by Djuth et al. [1994b]; this paper also includes a discussion of the advantages and limitations of the methodology. In the study presented here, the CLP-PEPL technique is employed to examine neutral wave motion in the lower thermosphere. An important feature of this technique is its ability to provide very accurate measurements of electron density throughout a large portion of the ionosphere (from ~110 km altitude to 500 km and beyond). As currently implemented at Arecibo, the technique yields electron density profiles with 150 m altitude resolution and 1-σ random error bars ranging from 0.01 to 0.03% after ~2.5 s temporal integration. In general, error bars near 0.03% are pertinent to observations made between 110 and 130 km altitude and at very high (>400 km) altitudes where the PEPL signal-to-clutter ratio is small.

For the Arecibo observations of interest here, the plasma line frequency (i.e. the Langmuir wave frequency, $\omega_r \equiv 2\pi f_r$) can be expressed to first order as

$$\omega_r^2 = \omega_{ep}^2 + \sin^2\theta\,\omega_{ec}^2 + \frac{3k^2\kappa T_e}{m_e}, \tag{1}$$

15

where ω_{ep} and ω_{ec} are the electron plasma frequency and electron cyclotron frequency, respectively, θ is the angle between the radar line-of-sight and the geomagnetic field, k is radar wavenumber, T_e is electron temperature, m_e is electron mass, and Boltzmann's constant is represented as κ. Worst case errors resulting from this approximation are of the order of 10 kHz, which are small compared to typical f_r values measured in the Arecibo ionosphere (3.5 MHz to >10 MHz). Radar echoes from PEPLs appear as narrow spectral peaks centered at 430 MHz + f_r and 430 MHz - f_r; the two peaks correspond to Langmuir wave vectors directed toward and away from the radar. In a homogeneous plasma, the spectral shape of the Arecibo plasma line is well-approximated by a Lorentzian having a full width at half maximum of γ/π, where γ is the intensity damping decrement of the Langmuir waves. The principal contributions to γ come from electron Landau damping and electron-ion/electron-neutral collisions. At thermal energies in the electron distribution function, Landau damping is a strong function of the radar viewing angle relative to the geomagnetic field. In the Arecibo F region, thermal Landau damping makes a dominant contribution to the overall damping decrement at frequency offsets from 430 MHz of $\lesssim 4$ - 5 MHz (depending on electron temperature). At greater frequencies, the damping decrement is determined by a combination of Landau damping from photoelectrons and collisional damping. Typically, PEPL spectral widths in a homogeneous plasma are ~200-400 Hz. From a practical standpoint, the spectral width of the F-region plasma line is usually determined by the vertical electron density gradient across the 150-m altitude cell. (A notable exception is the region near the F-region peak, where the vertical gradient is very small.) In the bottomside F region, ionospheric scale lengths are typically in the range of H = 50 - 100 km, where $H = n_o/[dn_e(z)/dz]$, $n_e(z)$ is electron density as a function of altitude z, and n_o is the electron density at the altitude of interest. The corresponding n_e gradients yield a spread in Langmiur wave frequency across a 150-m cell of the order of 4 - 8 kHz.

Absolute electron density (determined from ω_{ep}) is obtained by applying the magnetic-field and electron-temperature correction terms in (1) to measured values of f_r. Reasonably accurate values for θ and ω_{ec} can be obtained from geomagnetic field models. However, an independent determination of T_e is required to further refine the electron density measurement. This is readily accomplished with supplemental incoherent scatter observations at the so-called ion-line (backscatter centered at 430 MHz that is roughly 10-kHz in bandwidth.). If the T_e-correction term is neglected entirely, systematic electron density errors of ~3% result at heights near 110 km and decline to less than 1% at altitudes above 200 km. With the inclusion of the T_e measurements, systematic errors are less than 0.5% at all observation altitudes.

6.2 Radar Data Acquisition

The Arecibo radar data presented here were acquired in July 1992. The observing program made use of three types of radar pulses: a coded long-pulse (CLP) 512 μs in length with

1-μs bauds [*Sulzer*, 1986a]; a multiple-frequency radar pulse (308 μs in length) used for autocorrelation analyses (MRACF) [*Sulzer*, 1986b]; and a 13-baud Barker-coded pulse (BKR) having a baud length of 4 μs [e.g., *Gray and Farley*, 1973]. The three pulses were cyclically transmitted within a "frame time" of 30 ms. A frame consisted of three 10 ms interpulse periods (IPPs), one for each type of pulse. As noted above, the CLP is used with the PEPL to make very accurate measurements of electron density n_e with good altitude and temporal resolution. MRACF is the standard ion-line measurement program used to obtain electron temperature T_e, ion temperature T_i, ion-composition, and n_e at Arecibo. Such observations have excellent temporal resolution, but the effective altitude resolution is rather coarse (~38 km). BKR pulses produce an ion-line power profile (proportional to n_e) with high sensitivity and moderately good altitude resolution (600 m). The BKR observing program supplements CLP-PEPL measurements by extending altitude coverage of n_e to lower heights where PEPLs are not detectable. In addition, given the current 1-MHz transmitter bandwidth at Arecibo, BKR is more effective at detecting narrow ion layers than CLP-PEPL. This is discussed in greater detail below.

Standard incoherent scatter signal processing was employed for the MRACF and BKR observations [e.g., *Sulzer*, 1989]. In the case of CLP-PEPL, complex (in-phase and quadrature) voltages were sampled at a 5 MHz rate so that ~5-MHz segments of the plasma line spectrum could be covered. During the experiment, plasma line sidebands in the frequency range 430 MHz ± (3.5 to 8.5 MHz) were sampled. The low frequency limit (3.5 MHz) coincided with an electron Landau damping cutoff in signal strength; the high frequency limit (8.5 MHz) was set at the point where severe losses are encountered in antenna line-feed gain. This upper frequency restriction will be removed in the near future with the completion of the new wideband Gregorian feed system at Arecibo. Complex (in phase/quadrature) voltage data were digitized with 8-bit precision. Data acquired during each radar IPP are first decoded, range by range, to remove 1-μs phase transitions imposed on the time series. The combination of the 5 MHz sample rate and the 512-μs radar pulse generates 2,560 complex voltage samples for each 150-m range cell. Power spectra are formed by zero-padding the data samples to 4,096 points and then applying an FFT with a rectangular windowing function. In the current investigation, the Arecibo radar beam was pointed vertical and the peak transmitted power was ~1.6 MW. The results presented below were obtained at the downshifted plasma line (f_0 - f_r), where the sensitivity of the Arecibo line feed is the best.

6.3 Radar Observations

The results of *Djuth et al.* [1994b] provided the first indication that imprints of neutral waves in electron density profiles can be detected with the CLP-PEPL technique in the lower thermosphere. In response to these findings, a separate observing program was initiated at Arecibo Observatory specifically targeting the lower thermosphere for a more detailed

investigation. The results presented below were obtained on July 10, 1992 between 13:51 and 14:55 AST. They are typical of other observations made during a mini-campaign conducted from July 8 through July 10, 1992.

The BKR measurements presented in Figure 1 show the general shapes of the electron density profiles recorded during the observation period of interest. These observations provide altitude coverage below 110 km that is not available with the CLP-PEPL data. Each profile is the result of ~15 min of temporal integration (~30,000 consecutive BKR pulses). The profiles have been corrected for the effect of T_e/T_i [e.g., *Evans*, 1969] using MRACF data. However, the actual profile shapes may differ somewhat from those of Figure 1 because of inaccuracies in the ion composition model employed above ~145 km altitude (which affect deduced values of T_e/T_i) . In addition, there are uncertainties in the near-field antenna gain used to correct the profiles below ~130 km [*Djuth et al.*, 1994b]. The profiles reveal the presence of a small intermediate ion layer near 115 km altitude. Such layers have been studied in the past at Arecibo and are discussed in detail by *Mathews et al.* [1993].

In Figure 2, two examples of electron density profiles obtained with CLP-PEPL are displayed. One profile is averaged over the entire period of study (13:51 and 14:55 AST) while the other is obtained after a short 15-s integration period (500 CLP-PEPL pulses). Notice that the profile having a short integration period contains wave structure that is almost completely averaged out by the long-term integration. The long temporal average approximates mean background electron density profile. In order to highlight the electron density fluctuations, CLP-PEPL profiles were processed to remove the contribution from the "background" ionosphere. The background profile versus time was determined by fitting the electron density measured every 15 s at each altitude to a first order polynomial; the inclusion of a linear trend served to remove slow variations over time scales of an hour. In Figure 3, the electron density trend derived from the observations is displayed as a function of altitude.

A time series of residual profiles obtained after background profile subtraction is shown in Figures 4a - 4d. In these panels, electron density variations are expressed as a percentage relative to the background profile. The data of Figures 4a - 4d are not continuous from panel to panel; there are small temporal breaks of the order of 1 min between displays. These breaks were necessary for the storage of large (1 GB) data sets acquired every 15 min. (Continuous data acquisition is currently available for measurements of this type.) Temporal integrations of 15 s were selected for the displays of Figure 4 because no statistically significant changes in the profiles were detected over shorter time scales. Accurate CLP-PEPL profiles were available every 7.50 s, which corresponds to the integration of 250 pulses. If 250 consecutive pulses were used and partitioning of radar pulses among other observing techniques were not adopted, the corresponding temporal resolution would be 2.5 s. However, such short integration periods are
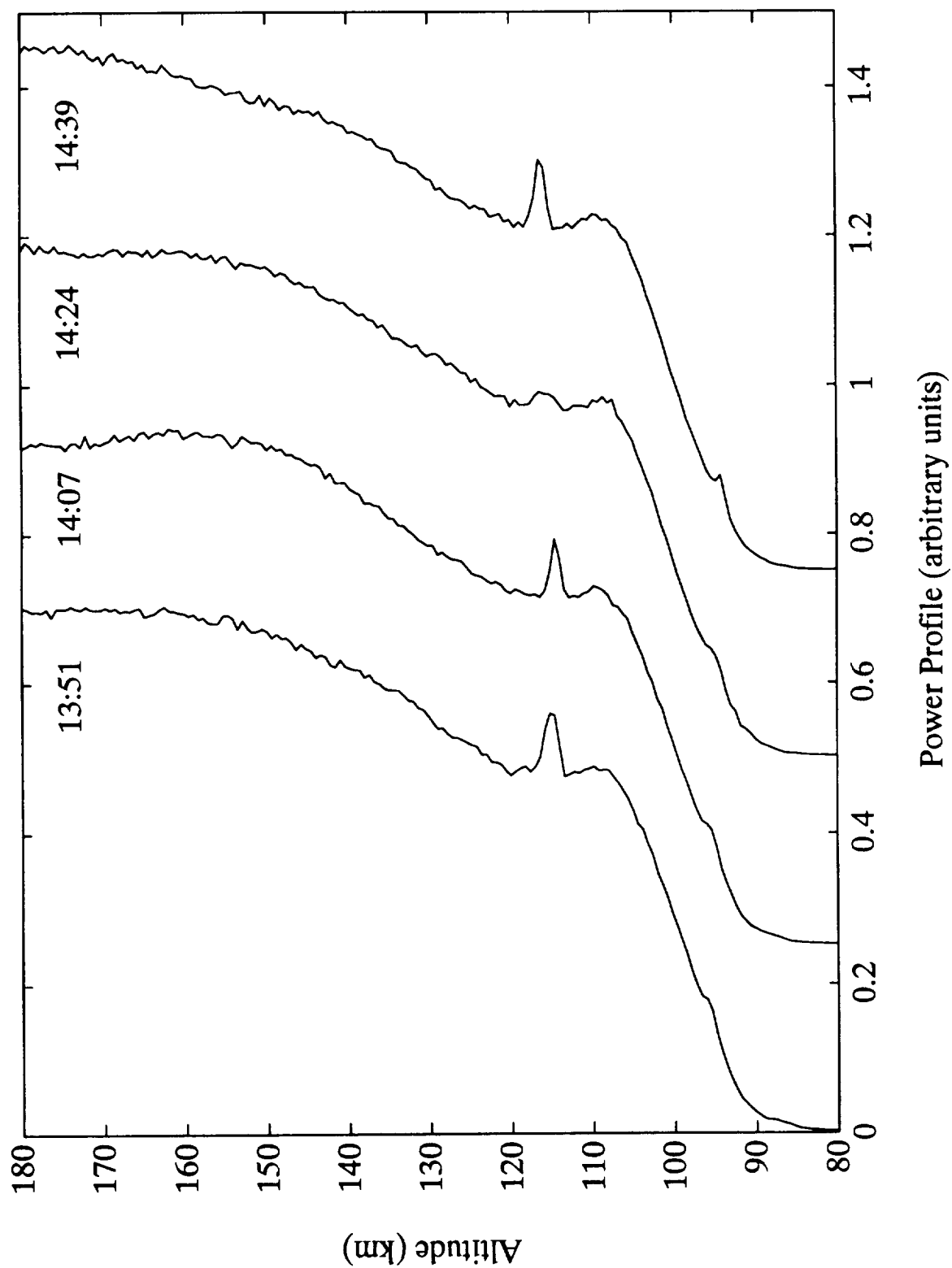
Figure 1. Incoherent scatter ion line profiles obtained at Arecibo Observatory between 13:51 and 14:55 AST on July 10, 1992. Each profile contains data integrated over a 15-min period. Integration start times are shown next to each profile.
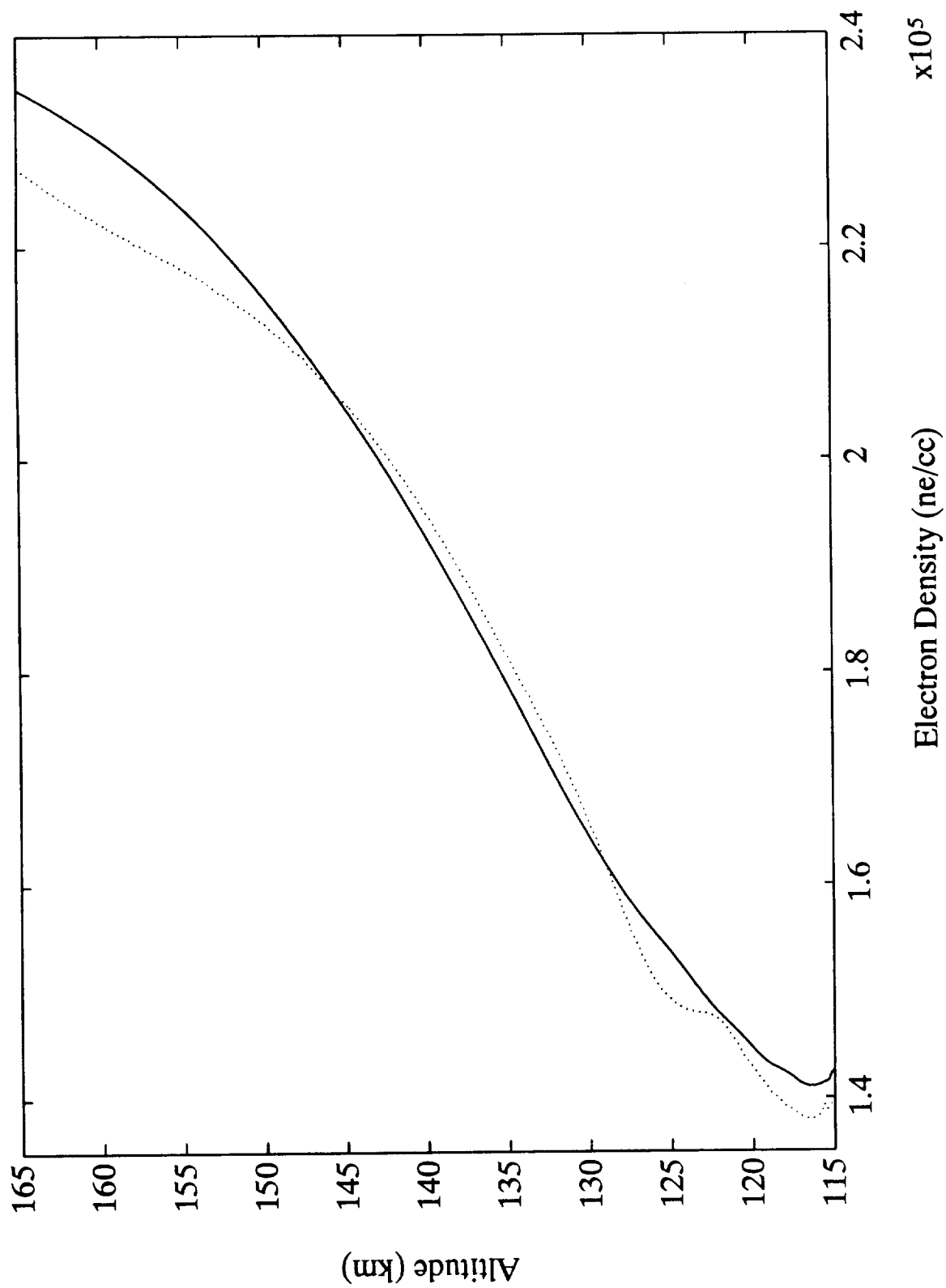
Figure 2. Electron density profiles obtained with plasma line measurements. A profile averaged over the time interval 13:51 - 1455 AST (solid line) is shown along with a 15-s average near 13:51 AST (dotted line).
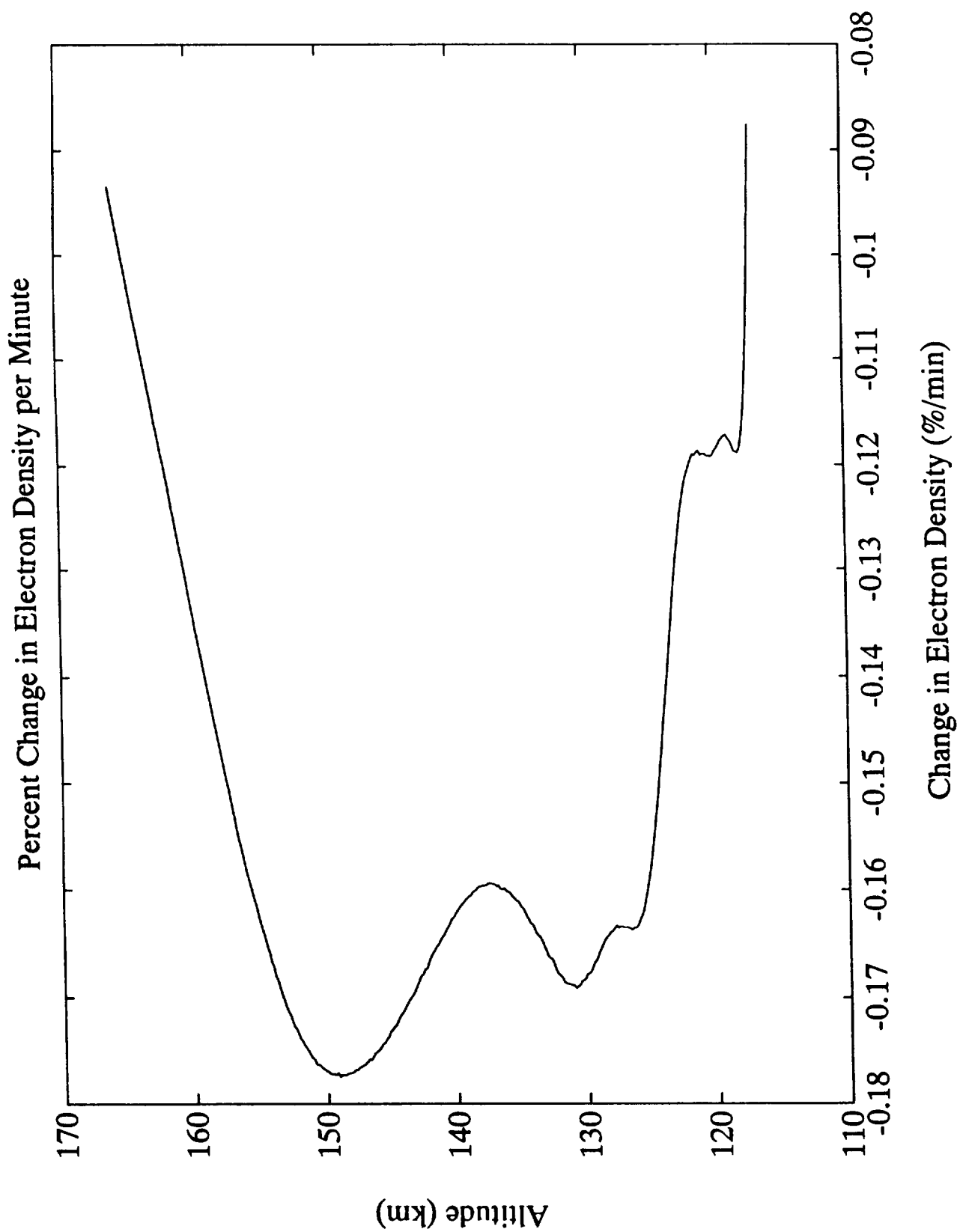
Figure 3. Temporal derivative of background electron density versus altitude for the period 13:51 - 14:55 AST on July 10, 1992. This rate of change is subtracted along with the mean electron density profile to obtain profile residuals.
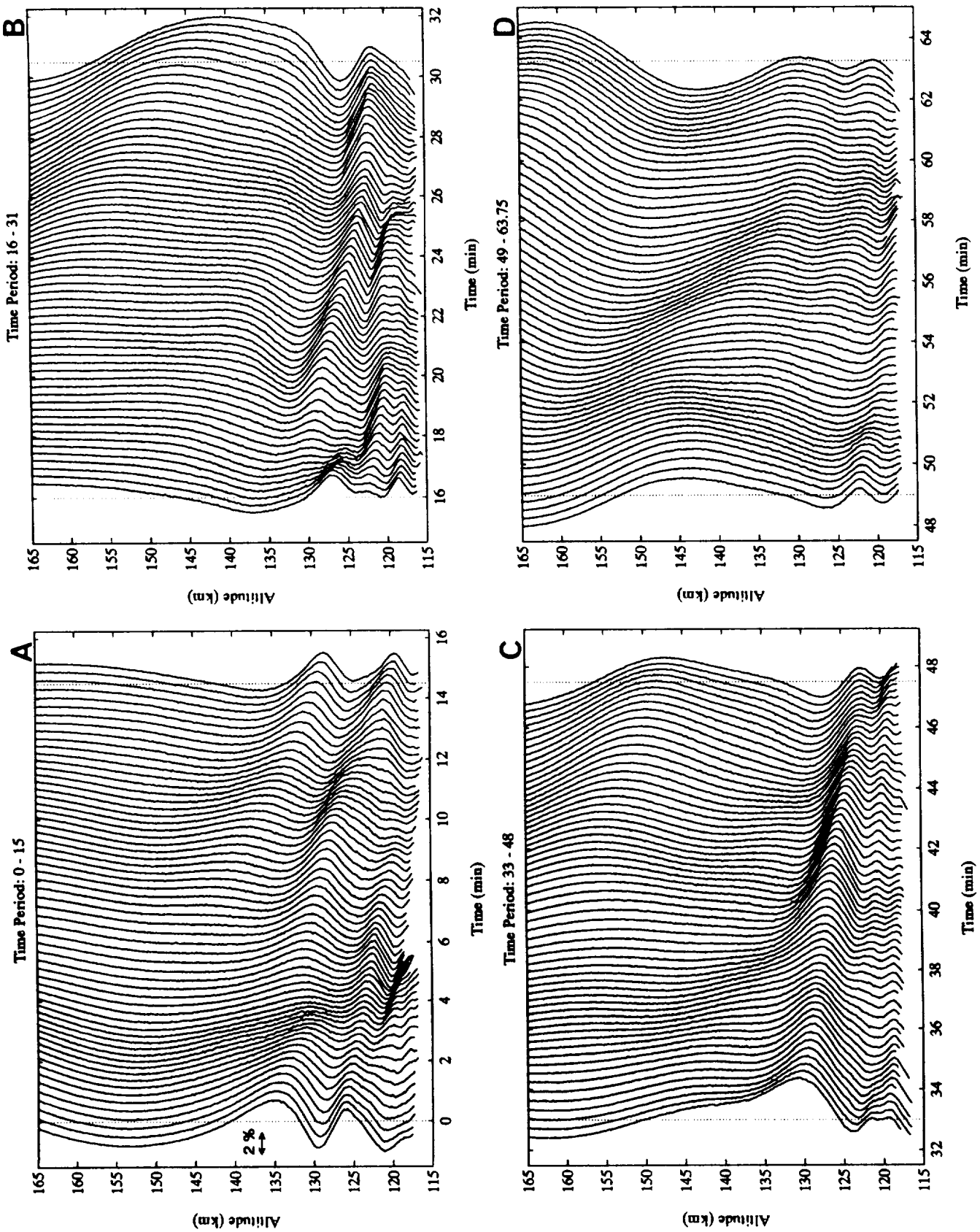
Figure 4. Residual electron density profiles expressed as a percentage of the mean profile. The vertical dotted lines in each panel denote the 0% fluctuation level for the first and last profiles. A double arrow near 0 min indicates the magnitude of a 2% fluctuation. Zero lines advance 15 s per profile. Time periods are in units of minutes and are referenced to 13:51:00 AST on July 10, 1992.

unnecessary for investigations of internal gravity waves. Conversely, studies involving acoustic waves in the upper atmosphere would benefit from such temporal resolution. An expanded view of the first profile of Figure 4b is provided in Figure 5 to expose fluctuations caused by random measurement errors. A 1% variation in electron density is detected at the significance level of 30 - 60 standard deviations (σ); σ is an altitude-dependent quantity linked to the signal-to-clutter ratio in a given range cell.

Two factors determined the altitude coverage of the observations in Figure 4. The upper altitude limit of the observations was set near 165 km to reduce the average data rate and thereby increase the time between temporal breaks in the data record. The low-altitude cutoff was dictated by the presence of an intermediate ion layer near 115 km (Figure 1). Steep electron density gradients associated with ion layers and sporadic-E regions greatly decrease the sensitivity of the Arecibo CLP-PEPL measurements. This is because a large change in electron density across the 150-m range cell widens CLP-PEPL spectral peaks, making nonlinear least-squares fitting difficult. Figure 6 shows the result of a long (150-s) temporal average of CLP-PEPL data at altitudes between ~110 and ~125 km. A faint outline of the intermediate ion layer is visible near 114.3 km altitude. The plasma line frequency profile continues below this into the upper E region. In the absence of the intermediate ion layer the signal strength would decline more gradually with decreasing altitude. The loss of signal at lowest altitudes near 110 km is brought about by increases in electron-neutral collision frequency, which increases the Langmuir wave damping decrement. Under solar minimum conditions, the Arecibo measurement capability improves at lower altitudes because of associated decreases in neutral density (and hence electron-neutral collision frequency). Altitude coverage can also be improved by increasing peak transmitted power. Substantial improvements were noted in 1993 when the Arecibo radar was operated at power levels $\geq$ 2 MW.

In general, CLP-PEPL plasma line work at Arecibo would greatly improve if the bandwidth of the 430 MHz transmitter were increased. In particular, significant gains would be realized if the 430 MHz transmitter could phase-code radar pulses at a 5 MHz rate instead of the existing 1 MHz rate. Independent spectra could then be obtained at 30-m range intervals without altering the current 5-MHz data sampling rate. In this case, the ratio of plasma line signal-to-(noise + clutter) would not change dramatically, but the altitude resolution would improve by a factor of five. The improved range resolution would sharpen the plasma line peaks and facilitate measurements across narrow ion layers. In the absence of narrow layers, the increase in the number of independent spectral measurements could be used to enhance the statistical accuracy of the measurements. Most importantly, spectra from consecutive altitudes could be averaged at lower altitudes to extend CLP-PEPL altitude coverage.
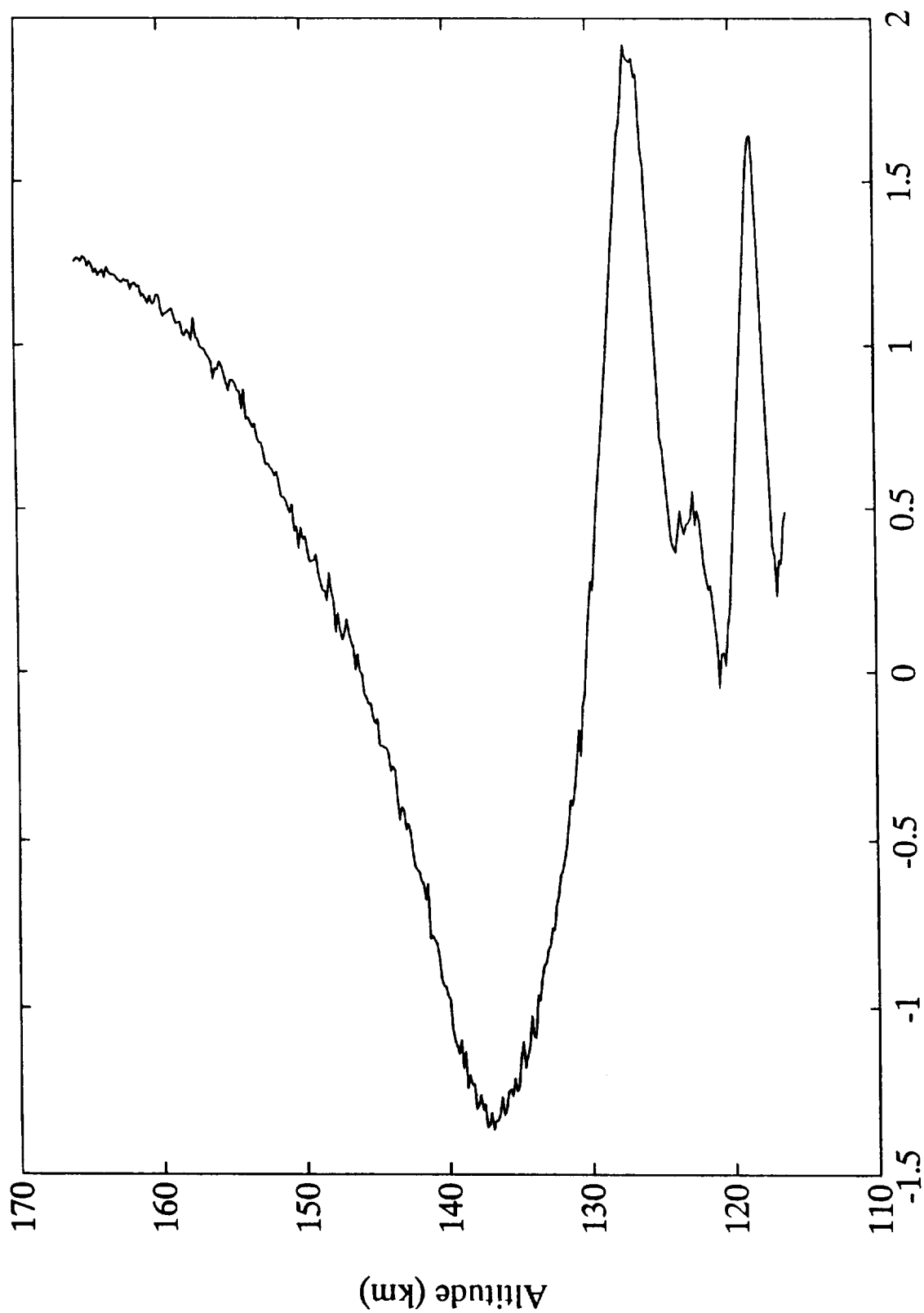
Percentage Difference of Electron Density

Figure 5. An expanded view of the first residual profile in Figure 4b. The point-to-point fluctuations superimposed on the altitude trends near 123 km altitude and above ~135 km are indicative of the measurement errors.
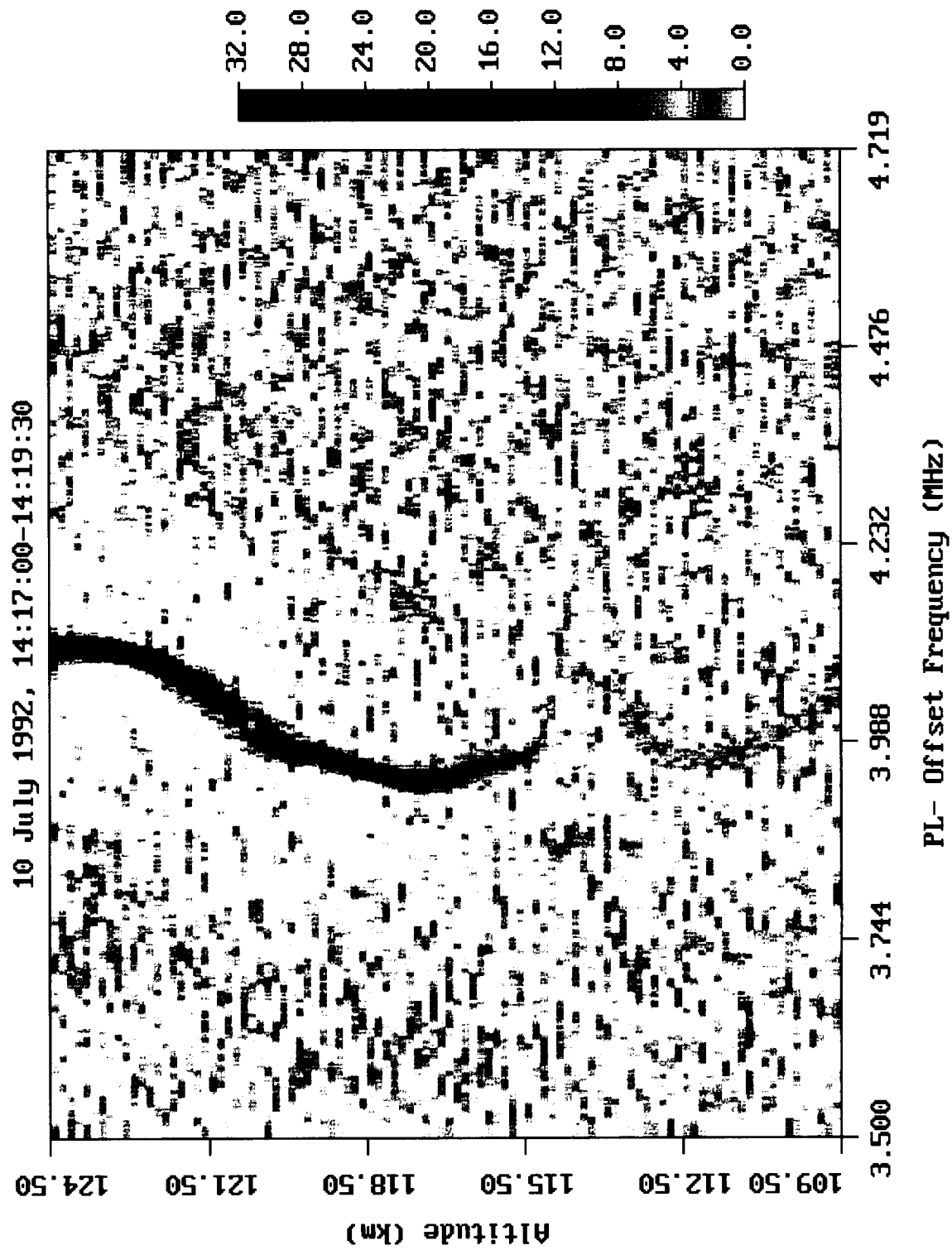
Figure 6. Intensity (linear scale) of the downshifted plasma line echo versus frequency offset from 430 MHz and altitude. The long (150 s) data integration period reveals the faint outline of an intermediate ion layer near 114.3 km altitude.

25

The wave structures shown in Figure 4 are clearly evident in all CLP-PEPL observations made to date at Arecibo. These include two mini-campaigns conducted in May, 1991 and July, 1992, and a more extensive campaign conducted in June/July, 1993. In addition the observed electron density variations appear to be distinct from the so-called "plasma rain" phenomena described by *Mathews et al.* [1996]. In this case, sheets of plasma descend from the bottomside ionosphere during evening/nighttime hours. These events exhibit a periodicity of ~8 min, but cannot be diagnosed with CLP-PEPL because of the absence of photoelectrons at evening hours.

It is interesting to note that the wave structures readily apparent with CLP-PEPL are very difficult to observe in standard ion-line profiles. If continuous BKR measurements were made, a 3-σ detection of a 2% electron density variation would require approximately 4 minutes of temporal integration. For waves having 10-minute periods, integration periods would span almost one-half of a fluctuation cycle. Nevertheless, efforts were made to implement the ion-layer detection strategy implemented by *Mathews et al.* [1993] and described in *Morton* [1991]. The algorithm entails the development of an inner envelope which is then subtracted from the BKR power profile to isolate peaks in the radar backscatter. When used with the BKR observations made jointly with the CLP-PEPL measurements of Figure 4, wave structures could not be detected. However, this technique was very effective at tracking the intermediate ion layer present near 115 km altitude (the intended purpose of the technique). Other approaches may be more effective in identifying wave structure along ion-line profiles, but no tests in this regard have been made to date. The key motivation for examining ion-line profiles is to extend the altitude coverage of wave activity to lower heights, even if the detection level is significantly reduced.

6.4 Analysis of Radar Results

The electron density structures of Figure 4 mirror several of the characteristics of internal gravity waves. Temporal periods are generally $\gtrsim$ 8-10 min, vertical half wavelengths are in the range of 2-25 km, and vertical wavelength continuously increases with altitude. In addition, the phase velocity of the wave-like perturbations is always directed downwards. Consequently, it is natural to examine these observations within the context of gravity wave theory. To determine essential gravity wave parameters, a model of the neutral atmosphere was developed using MRACF results to set the upper boundary condition. The neutral temperature T_n was set equal to the average T_i value (1029 K) measured at 187 km altitude. The MSIS-E90 model was then employed to determine neutral temperature, density, and mean molecular mass versus altitude. The model was forced to T_n=1029 K at 187 km by setting F10.7a = F10.7 = 174 for the day and time of the observations (July 10, 14:30 AST).

With the above neutral model, the Brunt-Väisälä frequency ω_g is calculated using the full expression [e.g., *Yeh and Liu*; 1974; *Väisälä*, 1925]:

$$\omega_g^2 = (\gamma - 1) g^2 / c_o^2 + (g / c_o^2) \partial(c_o^2) / \partial z \qquad (2)$$

where g (acceleration of gravity), γ (specific heat ratio), and c_o (sound speed) are all functions of altitude z. The characteristic period $\tau_g \equiv (\omega_g/2\pi)^{-1}$ ranges from 3.5 min (115 km altitude) to 7.8 min (165 km altitude). Because the mean horizontal ion drift was not measured during the Arecibo experiments, no attempt was made to include a Doppler shift originating from the background neutral wind in ω_g. Also of interest here is the theoretical minimum vertical half wavelength λ_z for internal gravity waves that are not subject to damping by kinematic viscosity [e.g., *Hines*, 1960; 1964a; 1974]. Calculated λ_z values range from 3 km (115 km altitude) to 30 km (155 km altitude).

To help quantify temporal periods, Fourier analyses were performed on the four continuous 15-min data segments displayed in Figure 4. Power spectra were calculated on an altitude by altitude basis. Each time series consisted of 60 data points that were zero-padded to 128 prior to the execution of a Fast Fourier Transform (FFT). The average of four power spectra, one for each panel of Figure 4, is shown in Figure 7. At altitudes below ~128 km, weak broadband noise is evident at frequencies between ~10 mHz and 33 mHz. This slight elevation in the noise floor is caused by increased measurement errors at the lowest heights. Spectral components of the atmospheric waves are confined to frequencies < 5 mHz. The -10 dB roll-off relative to the peak spectral power in a range cell is ~3 mHz (5.6 min period) at the lowest heights and ~2.5 mHz (6.7 min period) near 165 km; the -20 dB cutoff frequency varies from ~5 mHz (3.3-min period) at the lowest heights to ~4 mHz (4.2 min period) at the highest altitudes. Most of the spectral energy is located at periods in excess of τ_g consistent with the predictions of gravity wave theory.

Determinations of vertical half wavelengths from the observations are complicated by the fact that the perturbation wavelength rapidly increases with altitude. As a result, methods involving Fourier transforms of altitude series are not well-suited for this study. Two alternative approaches have been used to isolate vertical wavelength versus altitude: a zero-derivative analysis and a maximum entropy method. The former entails locating the maxima and minima of the density perturbations versus altitude by searching for zero vertical derivatives. Vertical half wavelengths are then estimated as the distance between adjacent maxima/minima; the altitude assigned to a vertical half wavelength is the midpoint between the maximum and minimum. To avoid the adverse impacts of random noise fluctuations, the data were fit to a second order polynomial in a step-wise fashion. The length of the fitted height interval increases with altitude to accommodate the increasing vertical wavelength. At the bottom of the density perturbation profile, a short data segment (±8 data points spanning 2.4 km) is fit to the quadratic; this fitting
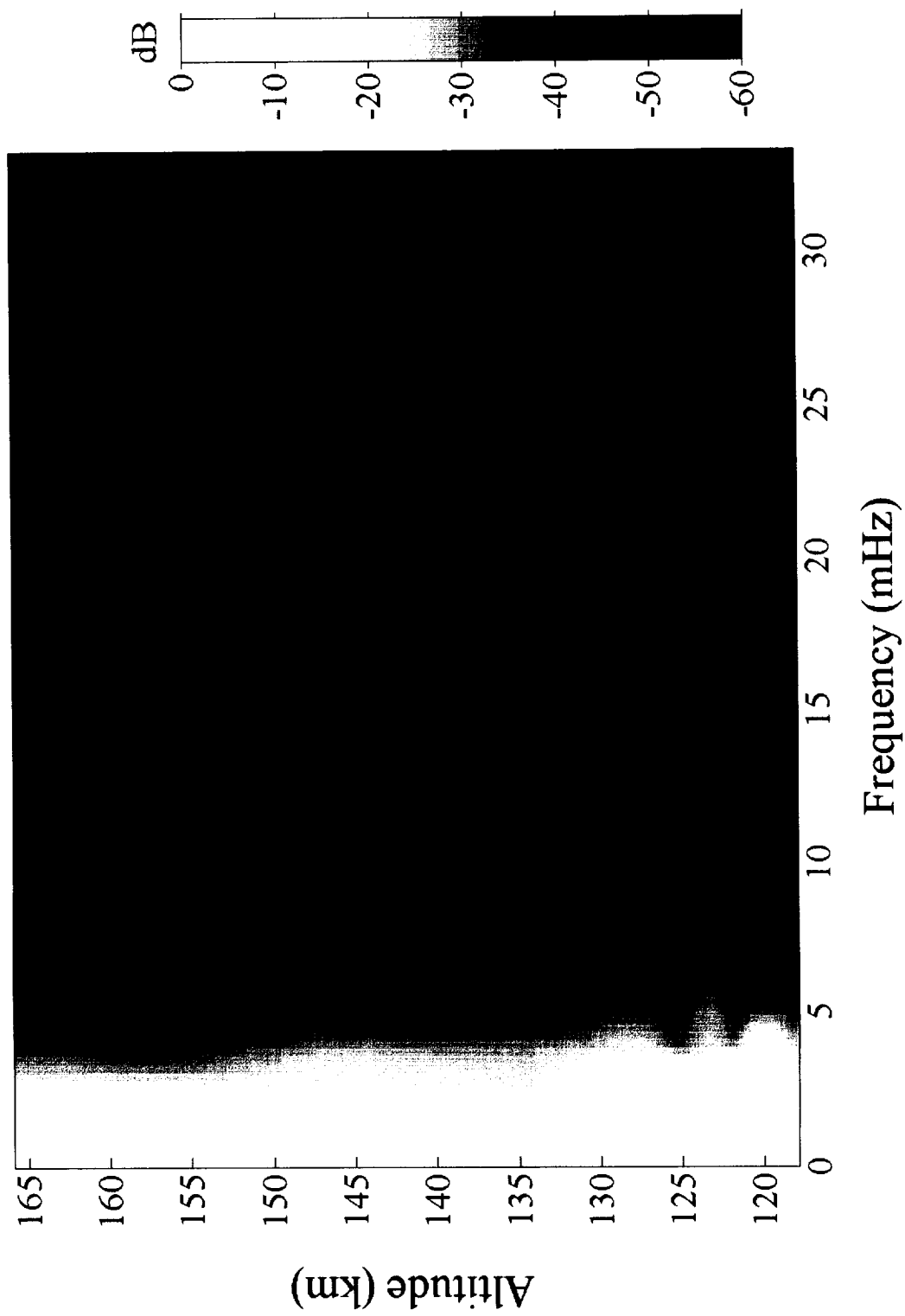
Figure 7. Fourier analysis of the electron density residuals of Figure 4. Power spectra versus altitude are calculated for each of the four panels in Figure 4. The average of the four panels is presented above.

interval increases linearly with altitude reaching ±35 points (10.7 km) at the highest altitudes. The center of the fitting interval is stepped up the entire profile, one altitude cell at time. Zero crossings of the vertical derivative are monitored versus altitude. When a zero crossing is detected, the corresponding altitude is stored along with the value of the fitted maximum or minimum. We define the amplitude of the vertical half wavelength perturbation as (maximum value - minimum value)/2. The results of the zero-derivative analysis is presented in Figure 8. Most of the waves below ~130 km altitude fall on the left side of the λ_z curve and are therefore quenched by kinematic viscosity. At higher heights, the waves are either unquenched or marginally quenched. A summary plot of the complete data set is provided in Figure 9. For the most part, the largest waves tend to reside near or to the right of the λ_z curve where damping is small.

In general, the zero-derivative analysis is most appropriate for a narrow-band wavenumber spectrum. For the most part, this appears to be applicable to the current observations. Nevertheless, difficulties can arise if the wavenumber spectrum broadens and exhibits structure. Multiple spectral peaks, in particular, could give rise to serious problems in the zero-derivative analysis. In order to avoid such problems, efforts were made to implement the Maximum Entropy Method (MEM) algorithm of *Burg* [1975] as outlined by *Press et al.* [1990]. Essentially, a model of the signal is constructed with parameters estimated from the data. The model is of the form:

$$P(f) = a_0 \left| 1 + \sum_{k=1}^{M} a_k z^k \right|^{-2} , \tag{3}$$

where P is power, f is spatial frequency, a_k are constants, and z is altitude. The MEM model contains poles that are useful in representing power spectra that have discrete lines or delta functions. This method has an advantage in that it can accurately model spectral peaks in cases where only a fraction of a wave cycle is present. Results from the zero-derivative and MEM techniques are illustrated in Figure 10. For comparison purposes, the MEM analysis was performed on data segments between minima and maxima selected via the zero-derivative technique. A continuous MEM analysis of vertical half wavelength versus altitude is provided in Figure 11. Reasonable agreement between the two techniques was realized in this test case. Unfortunately, for sinusoidal signals in noise, the Burg method exhibits a sensitivity to the initial phase of the sinusoid, particularly with respect to short data segments [e.g., *Proakis and Manolakis*, 1992]. In the current data set, this manifests itself as a frequency offset, or bias, from the "true frequency" that is dependent on the length of the data segment analyzed as well as the phase of the segment relative to the wave structure. Although MEM produces results consistent
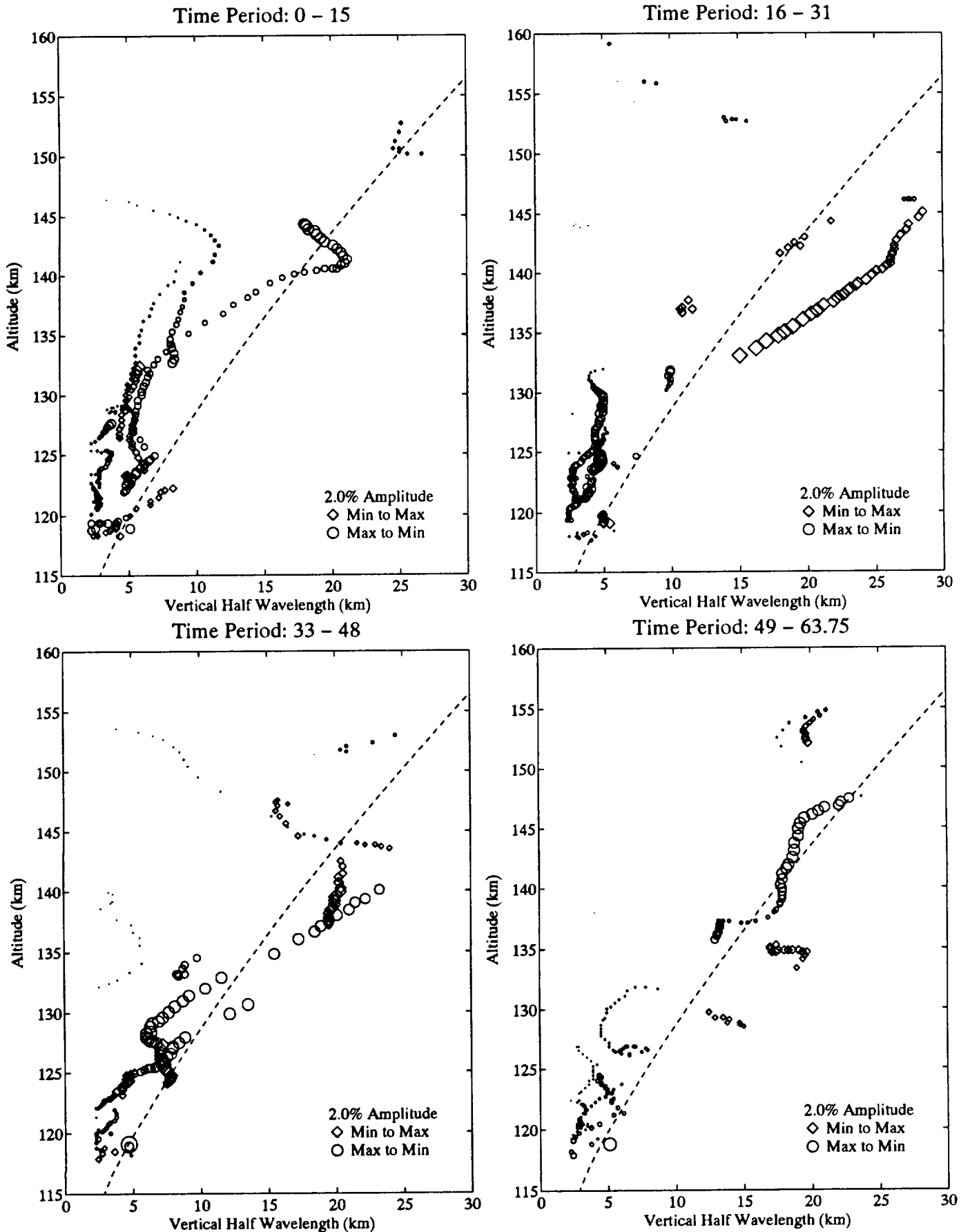
Figure 8. Vertical half wavelength versus altitude for the four observational periods of Figure 4. Measurements from the minima to maxima of n_e perturbations are shown as diamonds, whereas those from maxima to minima are represented as circles. Symbol sizes displayed at the bottom right of each panel correspond to a 2% amplitude fluctuation. The calculated curve for λ_z is plotted as a dashed line.
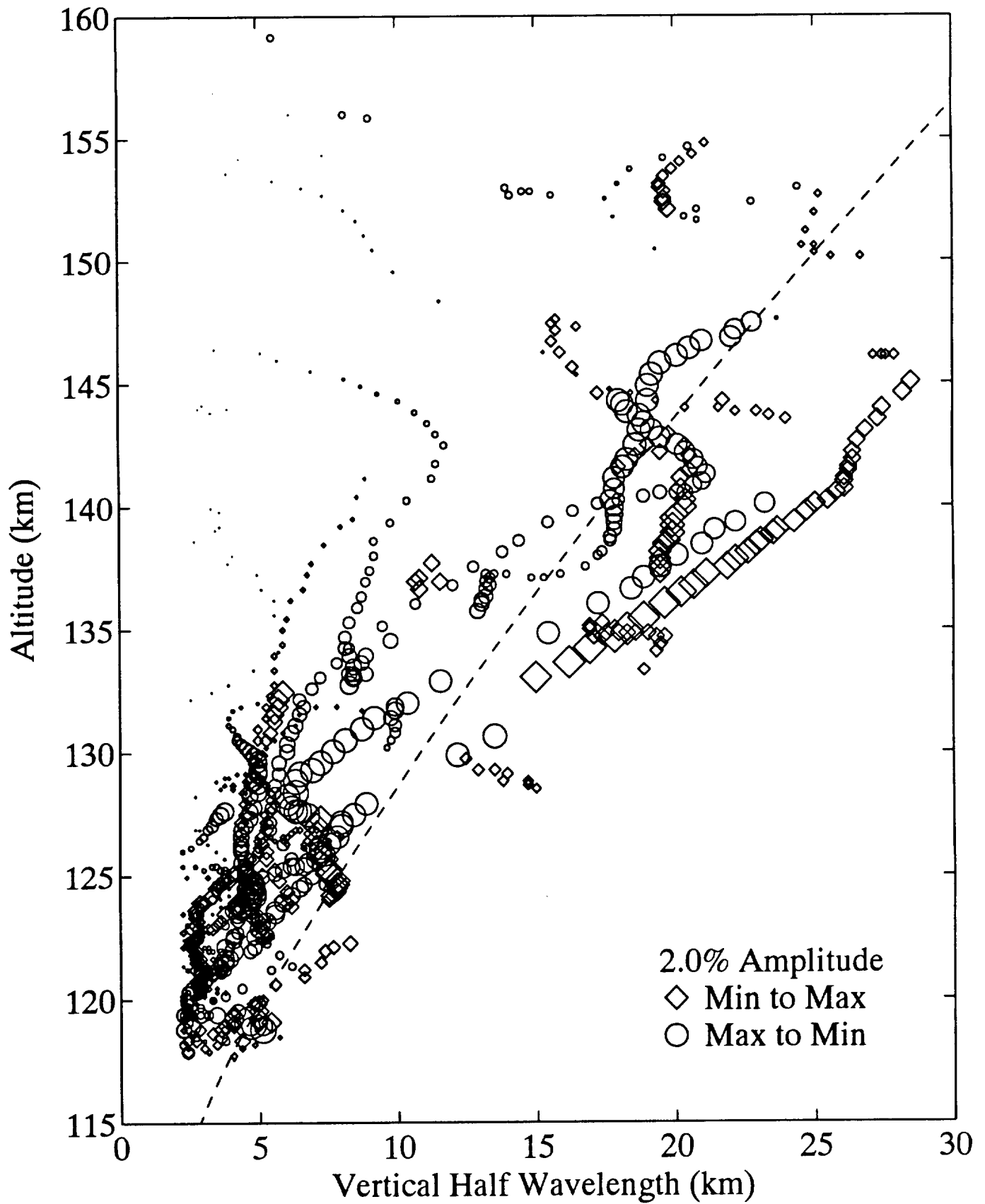
Figure 9. Cumulative plot of all results shown in the four panels of Figure 8.
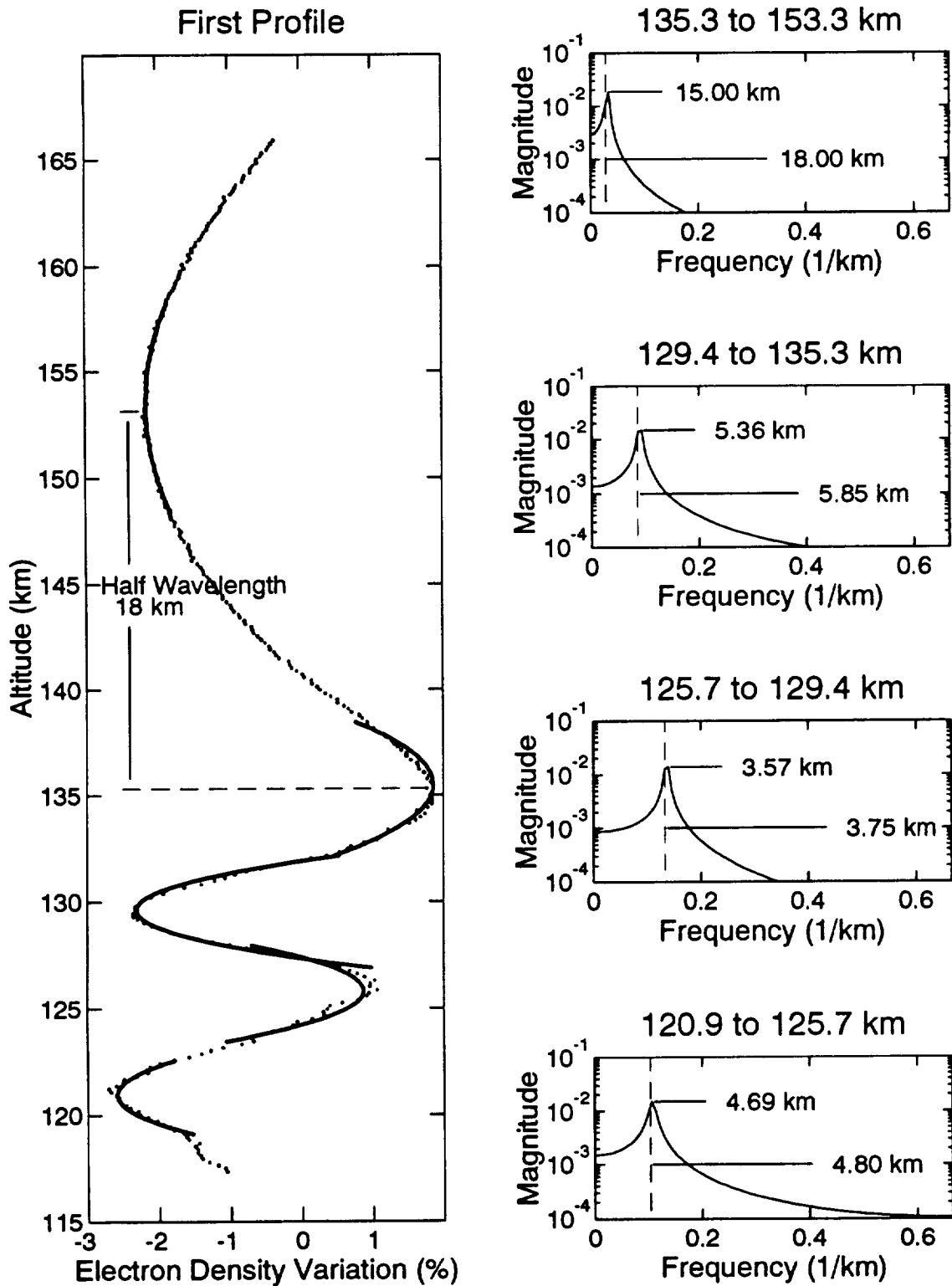
Figure 10. Comparison of zero-derivative and MEM techniques for deducing vertical half wavelength. Data from the first residual profile of Figure 4a are employed. The left panel illustrates the determination of zero-derivative locations using polynomial fits (bold curves) to the data points. The four panels at right show MEM spectra calculated for four altitude intervals over which zero-derivative results (vertical dashed lines) are obtained.

32
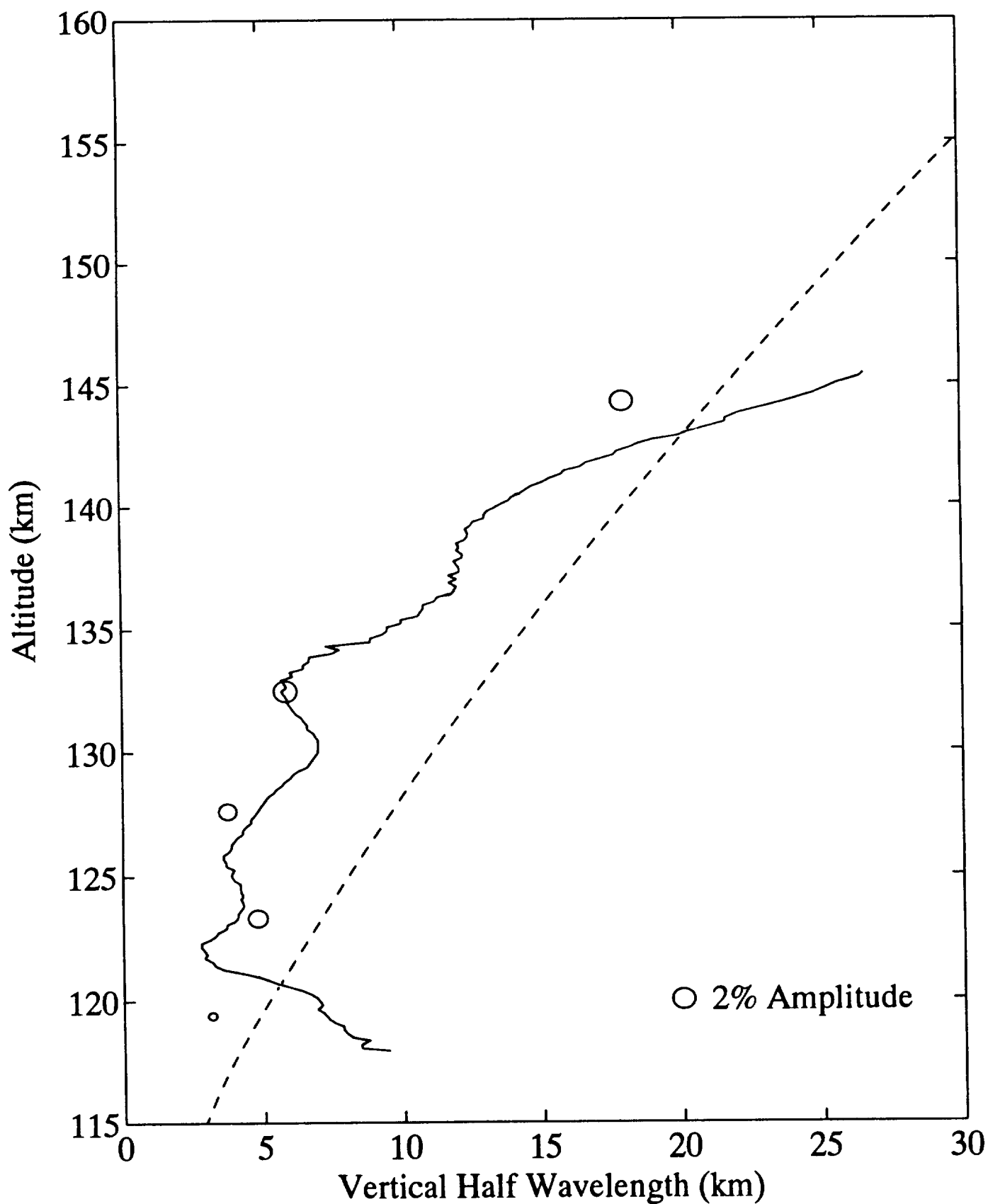
Figure 11. Comparison of zero-derivative results (circles) with MEM determinations (continuous line) of vertical half wavelength. Data from the first residual profile of Figure 4a are used in this example. The calculated curve for λ_z is plotted as a dashed line.

33

with the simpler zero-derivative analysis, extreme care must be exercised when it is used. This makes it very difficult to implement as part of an automated data-processing routine. Other analysis options need to be examined in the event that more complex (i.e. less clean) wave structures are detected at Arecibo.

6.5 Discussion of Results

It is clear that the temporal and spatial structures of the observed electron density perturbations exhibit several qualities characteristic of internal gravity waves. As noted in the preceding section, the frequency spectra exhibit a high-frequency cutoff consistent with calculated values of the Brunt-Väisälä frequency. Measured vertical wavelengths are not unlike those expected for internal gravity waves. However, if these wavelengths are directly related to gravity waves, some of the detected waves must be viscously damped. More generally, the vertical wavelengths of electron density perturbations increase with altitude, and the phase velocities of the corresponding waves are directed downwards in altitude. The observations appear to be consistent with plasma redistribution brought about by the passage of gravity waves through the ionosphere.

A simple model can be constructed to investigate the response of the ionosphere to neutral motions in the lower thermosphere. The goal is to determine how closely the observed electron density wave structure matches the neutral wind field and obtain a rough estimate of wind speed required to produce the density fluctuations. We begin with the assumption of a uniform plasma having a density of 2×10^5 cm^{-3}. In the actual observations, the electron density increases from ~1.45 $\times 10^5$ cm^{-3} at 115 km altitude to values near 2.35 $\times 10^5$ cm^{-3} at 165 km (see Figure 2). This relatively mild gradient is not included in the calculations. Ion/electron density fluctuations are modeled using the continuity equation with ion production and loss terms omitted. Dissociative recombination ($\propto N_e^2$, where N_e is electron density) is neglected because the amplitudes of the N_e perturbations are relatively small. The continuity equation reduces to:

$$\frac{\partial N_i}{\partial t} = -\text{div}(N_i V_i), \qquad (4)$$

where V_i is ion velocity, N_i is ion density. This equation describes the "sloshing" of the ionospheric plasma by the neutral gas. For vertical ion drifts at midlatitudes, we can set $N_i = N_e$ because of high electron mobility along the geomagnetic field. If we assume that the neutral vertical velocity U_z is zero, the vertical ion velocity V_z becomes [e.g., *Miller*, 1976; *Miller and Smith*, 1978] :

$$V_{iz} = [(\Gamma_x \Gamma_z + \rho_i \Gamma_y) U_x + (\Gamma_y \Gamma_z - \rho_i \Gamma_y) U_y] / (1 + \rho_i^2), \qquad (5)$$

where Γ is the geomagnetic field and U is neutral velocity, and x, y, and z correspond to east-west, north-south, and vertical components.

Figure 12 illustrates the ion response to neutral waves polarized in the geomagnetic east-west and north-south directions and at 45° (northeast-southwest) relative to these directions. In Figure 13, the associated electron density perturbations are displayed for a neutral wave having a 10 min period. The altitude profile for horizontal neutral velocity versus altitude was selected on the basis of the results of Figure 4. In the calculations, the assumed wind speed grows at a rate slightly less than the undamped rate, $\exp(z/2H)$, where H is the neutral scale height. Thus, a light damping term was added. This was done to reproduce the approximate amplitudes of the observed electron density perturbations. It is also consistent with the fact that many of the observed waves have λ_z values indicative of mild quenching. However, our aim here is not to deduce the precise background winds responsible for the observations. Additional measurements are required before such a task can be attempted.

As expected, Figure 12 shows that the N-S neutral wind dominates ion vertical motion at altitudes above ~130 km whereas the E-W wind is dominant below 130 km. The hybrid case of 45° is most effective at driving ion vertical motion throughout the 110-180 km altitude interval. In general, the rate of change of ion density $(-\text{div}(N_i V_i))$ is the greatest near the null point of the neutral wind field leading to reductions and enhancements in ion density. This is similar to models of horizontal plasma structure in sporadic E driven by gravity waves [e.g., *Hines*, 1964b; Hines 1965]. In the case of a N-S wind, there is a slight upward displacement between the null in the neutral wind and points of maximum and minimum $(-\text{div}(N_i V_i))$. This occurs because the vertical motion imparted to the ions by the neutral gas significantly increases with altitude. The displacement is smaller for E-W winds because the gradient in the envelope of vertical ion velocity is smaller. A slight displacement may also arise for a wave at 45° for the above reason as well as because of the transition from dominant forcing by E-W winds below ~130 km to dominant N-S forcing above.

Equation (4) can easily be solved to determine the resulting ion/electron perturbation. Results for a neutral wave having a period of 10 min are shown in Figure 13. The assumed altitude profile of the neutral wind field is the same as that in Figure 12. Calculations are presented for the case of a 45° wind. The plasma perturbations above ~120 km altitude are of the order of ± 2%, which conforms to the observations. Thus, it appears that horizontal wind fluctuations of only 2-4 m/s are necessary to account for the measured electron density perturbations.

Overall, the vertical wave structure of the electron density perturbations tends to follow the vertical wavelength of the wind field. However, as noted above, small differences exist because of the electrodynamic coupling of the magnetized ion gas to the neutral gas. This effect is most significant at altitudes between 110 km and 140 km. At higher altitudes, the N-S wind
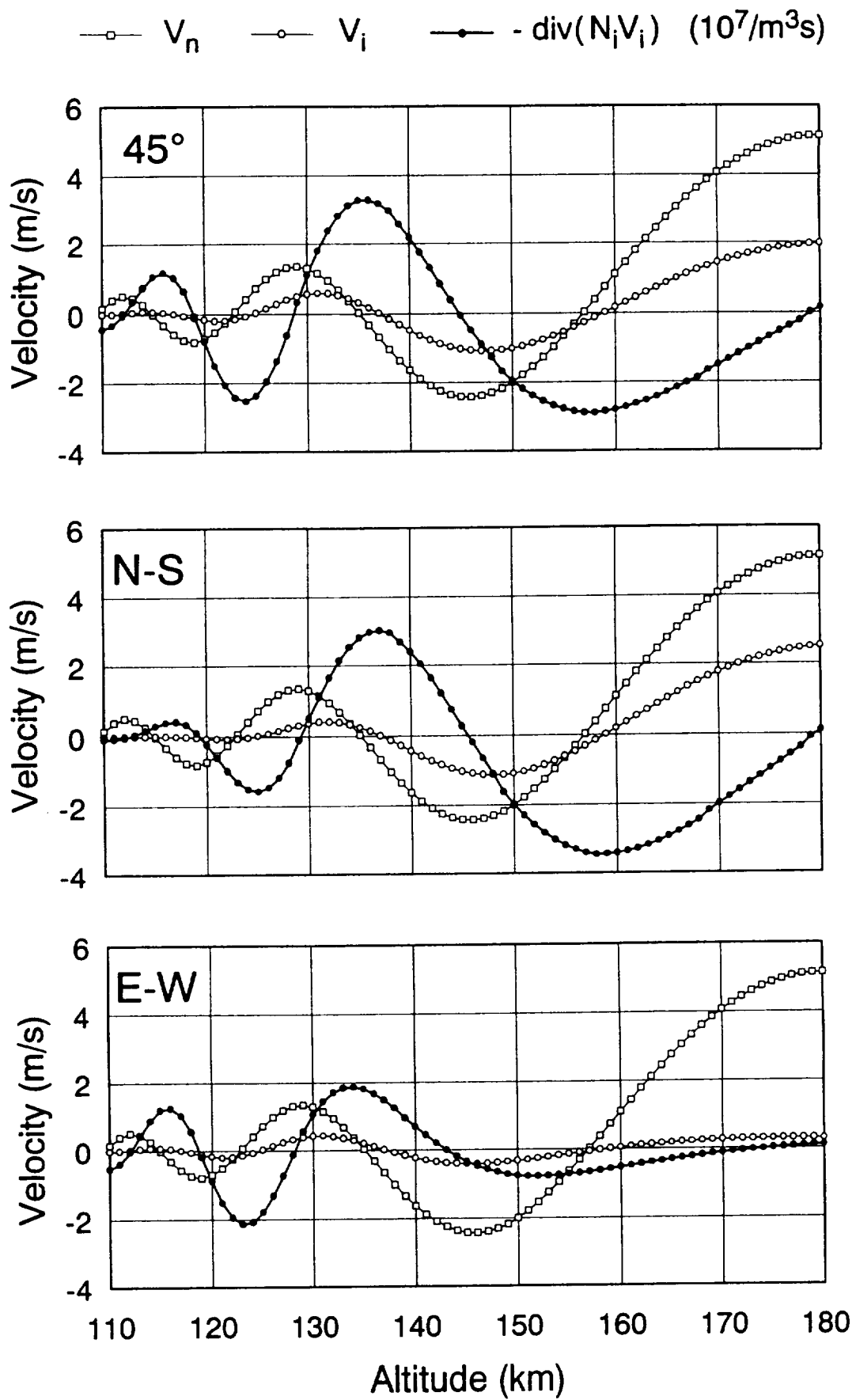
Figure 12. Vertical ion response to neutral waves horizontally-polarized in the geomagnetic northeast-southwest (45°), north-south (N-S), and east-west (E-W) directions. V_n refers to horizontal neutral velocity, whereas vertical ion velocity is designated as V_i.
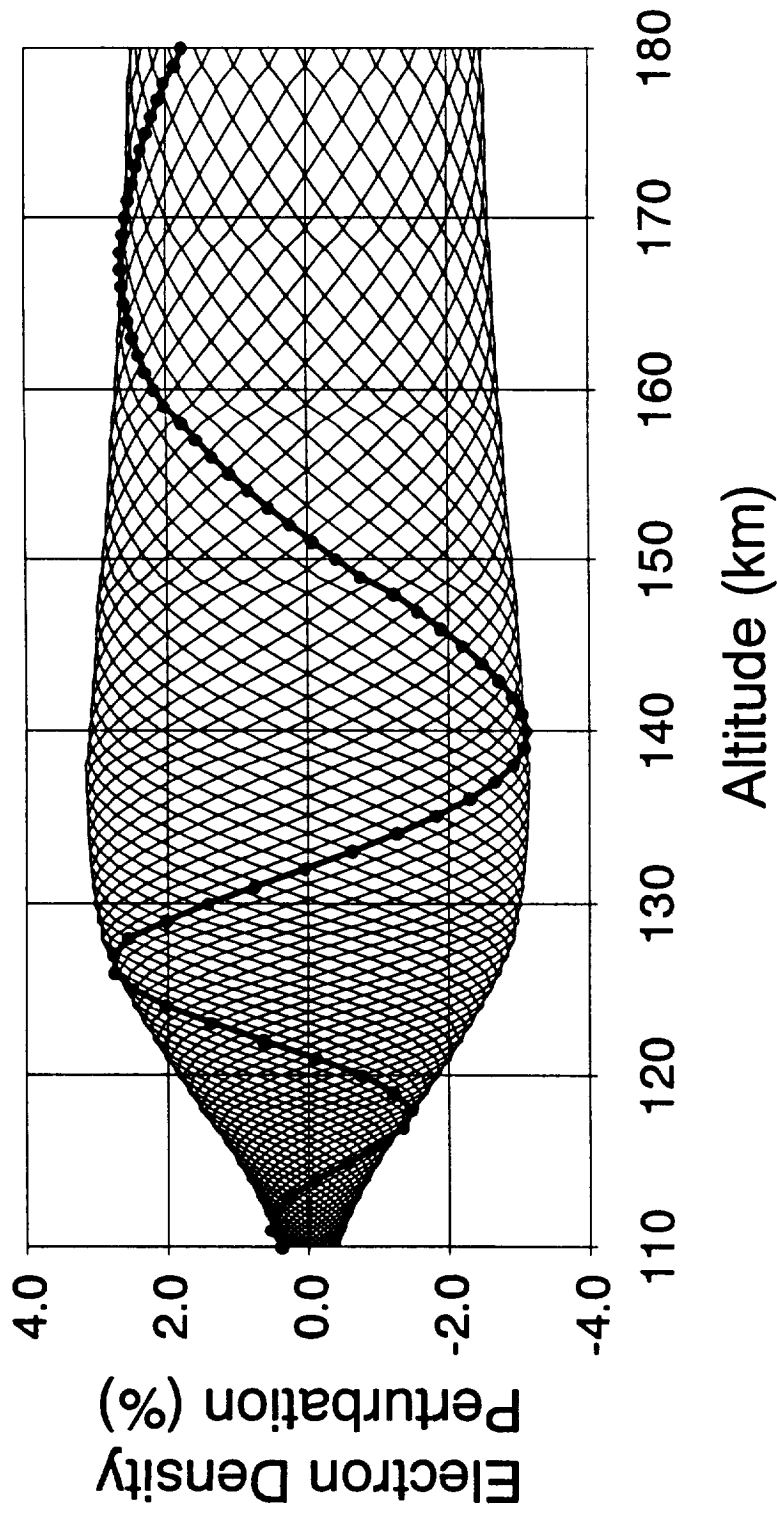
Figure 13. Electron density fluctuations calculated for the 45° neutral wind field of Figure 12 with a 10 min period. Waves separated in phase by 12° are shown for the full period. The envelope of electron density perturbations versus height is evident in the display; a single wave is highlighted for reference.

component dominates the plasma redistribution process, and the electron density imprints closely match the N-S vertical wind field structure of the gravity wave.

Additional data obtained in 1993 extended the coverage of the plasma line measurements to very high altitudes above 550 km. In Figure 14, an electron density profile averaged over a 5-min period is shown over an altitude interval beginning at 110.8 km and ending at 583.3 km. These measurements were made at the downshifted plasma line where the 430 MHz line feed is most sensitive to plasma line echoes. Nevertheless, at plasma line frequencies near 430 MHz - 8 MHz the line feed losses are ~3 dB greater than at 430 MHz, and these losses rapidly increase with increasing frequency offset from 430 MHz. Moreover, the plasma line signals encounter additional losses as they move outside of the 5-MHz Gaussian filter used in the experiment. The nominal bandpass of the filter extended from 430 MHz-3 MHz to 430 MHz-8 MHz. Thus, the plasma line signal strengths used to construct Figure 14 become progressively weaker near the F-region peak where the plasma line frequency is greater than 8.5 MHz. At the peak itself, the plasma lines are too weak to distinguish the echo peak from the noise. The dashed line shown in Figure 14 near the F-region peak is an interpolation based on a spline fit to data points near the peak. It is worth noting that the 430 MHz line feed losses at large plasma line frequencies will be eliminated with the completion of a new wideband Gregorian feed at Arecibo.

Figure 15 shows residual electron density profiles obtained after subtraction of the mean electron density profile calculated from the observations of Figure 14. Twenty residual profiles are displayed; each profile spans an interval of 15 s. Residuals are expressed as a percentage of mean electron density. For the purposes of presentation, each residual profile is displaced 2% to the right. Ideally, the observations of Figure 15 would benefit from the subtraction of a mean profile with a linear trend established over the course of an hour. However, these measurements were made in support of studies of electron thermal balance in the ionosphere which was not well-served by long data acquisition cycles. Nevertheless, the data of Figure 15 clearly illustrate the existence of wave activity at altitudes as high as 500 km. The electron density imprints become very small at the highest altitudes because of viscous (molecular/hydrodynamic) damping of the associated neutral waves.

6.6 Summary

The coded long pulse technique discussed above was originally developed for use with the standard incoherent scatter "ion line" echo and for use with the enhanced plasma line monitored during HF ionospheric modification experiments [*Sulzer*, 1986a, 1989]. Early tests with the HAARP data acquisition system entailed the use of the coded long-pulse technique with echoes from the natural ion line and the photoelectron-enhanced plasma lines [*Djuth et al.*, 1994b]. The radar processors proved to be fast enough to capture the full information content of the Arecibo 430 MHz radar. The ensuing investigations focused on the photoelectron-enhanced plasma line
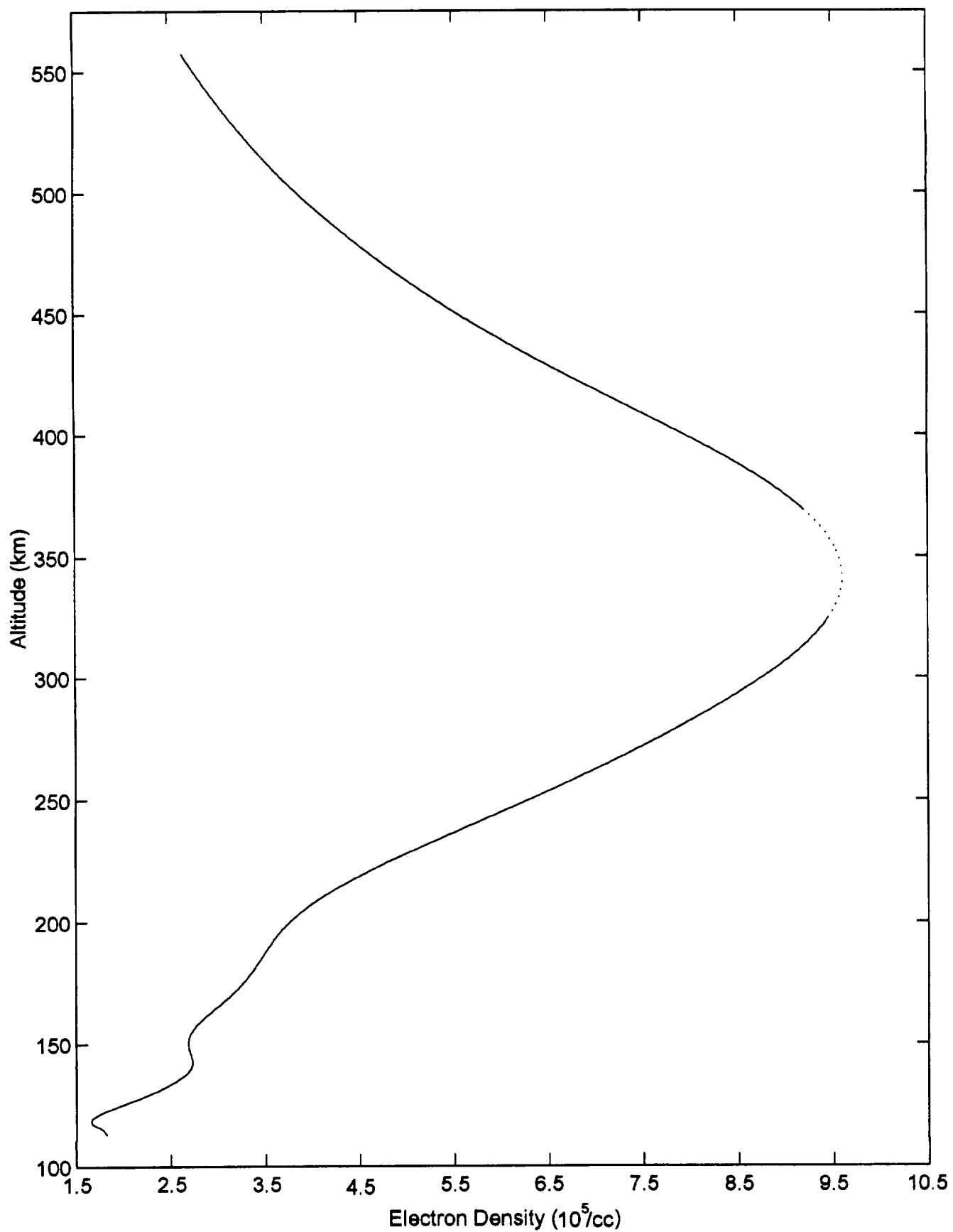
Figure 14. Mean electron density profile obtained 1 July 1993, 12:03 - 12:08 AST.
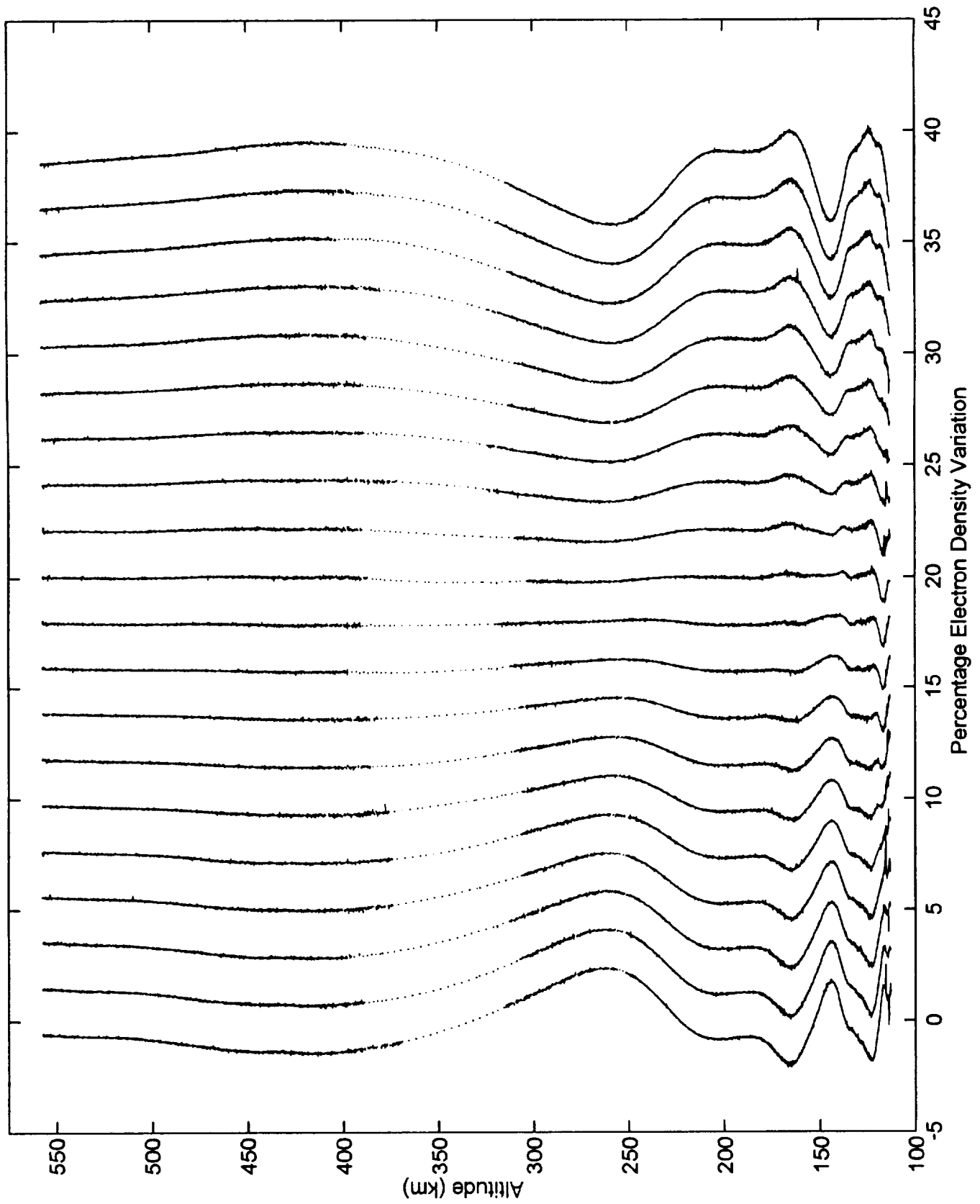
Figure 15. Electron density residuals measured over an extended altitude interval. Twenty profiles obtained during a 5-min observation period are displayed. Each profile is stepped to the right by 2% in electron density variation.

because it was believed that the high-resolution profile measurements would foster a significant amount of spin-off science. The illustrative example provided in this section is one of many studies that have proven this point.

The exploratory research presented above shows that the Arecibo radar can be routinely used to detect electron density imprints of internal gravity waves throughout the thermosphere. Gravity waves can be tracked as high as 500 km altitude. The observed waves exhibit a relatively narrow spectrum of vertical wavenumbers. About one-half of the waves detected in the lower thermosphere have vertical wavelengths short enough to be quenched. The horizontal neutral wind perturbations that give rise to the electron density imprints in the lower thermosphere are relatively small (2-4 m/s). In this regard, the Arecibo radar may be detecting leakage from the breakdown/supersaturation of gravity waves in the mesosphere. Additional modeling of this type of observation may allow the vertical energy flux of gravity waves to be deduced at Arecibo.

BIBLIOGRAPHY

Balsley, B. B., and W. L. Ecklund, *IEEE Trans. Antennas & Propagation, AP-20*, 513-516, 1972

Bernhardt, P. A., C. L. Siefring, P. Rodriguez, D. G. Haas, M. M. Baumback, H. A. Romero, D. A. Solin, F. T. Djuth, L. M. Duncan, D. E. Hunton, C. J. Pollock, M. P. Sulzer, C. A. Tepley, L. S. Wagner, and J. A. Goldstein, The ionospheric focused heating experiment, *J. Geosphys. Res., 100*, 17331-17345, 1995.

Burg, J. P., Maximum Entropy Spectral Analysis, Ph.D. thesis. Stanford University, Department of Geophysics, 1975.

Djuth, F. T., Nonlinear resonance effects produced in the *F* region by high-power radio waves, *The Review of Radio Science 1990-1992*, ed. W. R. Stone, Oxford University Press, Chapter 29, 601-610, 1993.

Djuth, F. T, P. Stubbe, M. P. Sulzer, H. Kohl, M. T. Rietveld, and J. H. Elder, Altitude characteristics of plasma turbulence excited with the Tromsø superheater, *J.Geosphys. Res., 99*, 333-339, 1994a.

Djuth, F. T., M. P. Sulzer, and J. H. Elder, Application of the Coded Long Pulse Technique to Plasma Line Studies of the Ionosphere, *Geophys. Res. Lett., 21*, 2725-2728, 1994b.

Djuth, F. T., M. P. Sulzer, J. H. Elder, and K. M. Groves, The CRRES AA 2 release: HF wave-plasma interactions in a dense Ba$^+$ cloud, *J. Geophys. Res., 100*, 17347-17366, 1995.

Djuth, F. T., J. H. Elder, and K. L. Williams, Auroral and Midlatitude Radar Studies: Radar Methods for Improved Diagnostics of the HF-modified and Natural Ionospheres, Phillips Laboratory Report PL-TR-96-2070, 66 pp., 1996a.

Djuth, F. T., M. P. Sulzer, and J. H. Elder, Electron density imprints of gravity waves in the lower thermosphere, *J. Geophys. Res.*, submitted, 1996b.

Djuth, F. T., M. P. Sulzer, and J. H. Elder, Detection of artificial plasma inhomogeneities in HF modification experiments at HIPAS, *J. Geophys. Res.*, submitted, 1996c.

Evans, J. V., Theory and practice of ionosphere study by Thomson scatter radar, *Proc. IEEE, 57*, 495-530, 1969.

Fejer, J. A., F. T. Djuth, and C. A. Gonzales, Bragg backscatter from plasma inhomogeneities due to a powerful ionospherically reflected radio wave, *J. Geophys. Res., 89*, 9145-9147, 1984.

Fejer, J. A., M. P. Sulzer, and F. T. Djuth, Height dependence of the observed spectrum of radar backscatter from HF-induced ionospheric Langmuir turbulence, *J. Geophys. Res., 96*, 15,985-16,008, 1991.

Gray, R. W., and D. T. Farley, Theory of incoherent-scatter measurements using compressed pulses, *Radio Sci., 8*, 123-131, 1973.

Hines, C. O., Internal atmospheric gravity waves at ionospheric heights, *Can. J. Phys., 38*, 1441-1481, 1960.

Hines, C. O., Minimum vertical scale sizes in the wind structure above 100 kilometers, *J. Geophys. Res.*, *69*, 2847-2848, 1964a.

Hines, C. O., The formation of mid-latitude sporadic-*E* layers, *J. Geophys. Res.*, *69*, 1018-1019, 1964b.

Hines, C. O., Motions of the neutral atmosphere, in *Physics of the Earth's Upper Atmosphere*, edited by C. O. Hines, I. Paghis, T. R. Hartz, and J. A. Fejer, pp. 134-156, Prentice-Hall, Englewood Cliffs, NJ, 1965.

Hines, C. O., *Paper 13*, in *Upper Atmosphere in Motion, Geophysical Monograph 18*, edited by C. O. Hines, pp. 429-441, American Geophysical Union, Washington, DC, 1974.

Mathews, J. D., Y. T. Morton, and Q. Zhou, Observations of ion layer motions during the AIDA campaign, J. Atm. Terr. Phys., *55*, 447-457, 1993.

Mathews, J. D., M. P. Sulzer, and P. Perillat, Aspects of layer electrodynamics revealed by high-resolution ISR observations of the 80-270 km ionosphere, *Geophys. Res. Lett.*, submitted, 1996.

Miller, K. L., and L. G. Smith, Horizontal structure in midlatitude sporadic-*E* layers observed by incoherent scatter radar, *Radio Sci.*, *10*, 271-276, 1975.

Miller, K. L., and L. G. Smith, Incoherent scatter radar observations of irregular structure in mid-latitude sporadic *E* layers, *J. Geophys. Res.*, *83*, 3761-3775, 1978.

Morton, Y. T., Ion layers, tides, gravity waves, and electric fields in the upper atmosphere inferred from Arecibo incoherent scatter radar measurements, Ph.D. thesis. The Pennsylvania State University, Department of Electrical and Computer Engineering, 1991.

Press, W. H., B. P. Flannery, S. A. Teukolsky, and W. T. Vettering, *Numerical Recipes, The Art of Scientific Computing*, 702 pp., Cambridge University Press, New York, 1990.

Proakis, J. G., and D. G. Manolakis, Digital Signal Processing: Principles, Algorithms, and Applications, 969 pp., Macmillan, New York, 1992.

Sulzer, M. P., A radar technique for high range resolution incoherent scatter autocorrelation function measurements utilizing the full average power of klystron radars, *Radio Sci.*, *21*, 1033-1040, 1986a.

Sulzer, M. P., A phase modulation technique for a sevenfold statistical improvement in incoherent scatter data-taking, *Radio Sci.*, *21*, 737-744, 1986b.

Sulzer, M. P., Recent incoherent scatter techniques, *Adv. Space Res.*, *9*, (5)153-(5)162, 1989.

Thidé, B., F. T. Djuth, H. M. Ierkic, and T. B. Leyser, Evolution of Langmuir turbulence and stimulated electromagnetic emissions excited with a 3-MHz pump wave at Arecibo, *J. Geophys. Res.*, *100*, 23887-23899, 1995.

Väisälä, V., Über die Wirkung der Windschwankungen auf die Pilot Beobachtungen, *Comment. Phys. Math. II*, *19*, 37, 1925.

Yeh, K. C., and C. H. Liu, Acoustic-gravity waves in the upper atmosphere, *Rev. Geophys. Sp. Phys.*, *12*, 193-216, 1974.

Yngvesson, K. O., and F. W. Perkins, Radar Thomson scatter studies of photoelectrons in the ionosphere and Landau damping, *J. Geophys. Res.*, *73*, 97-110, 1968.

Appendix A - HAARP Equipment Listing

Listing of HAARP Diagnostics Procured Under Contract NAS8-39238.					
Date	Vendor	Description	Cost	Tag	Serial Number
12/16/91	Trak	Time Code Processor	$4,031	N2-1	323
01/05/92	Metrum	Instrumentation Recorder	$57,745	N2-2	0103543KH91
03/31/92	Metrum	Preamp switch kit, instrument. recorder opt. 1	$458	N2-2	none
04/16/92	Metrum	Direct Record Boards, instrument. recorder opt. 2	$1,519	N2-2	16781252-146
01/31/92	Tektronix	2465B Scope	$6,072	N2-3	B059013
12/16/91	Fluke	Pulse Generator PM5716	$3,807	N2-4	SM524902
12/16/91	Fluke	Pulse Generator PM5716	$3,807	N2-5	SM524903
04/15/92	Fluke	PM3094 4 Ch. Scope	$3,397	N2-6	DM546022
02/21/92	HP	3589A Spectrum/Net An	$20,554	N2-7	3129A00238
12/16/91	Fluke	Pulse Generator PM5716	$3,807	N2-8	SM524904
02/01/92	Tektronix	TDS540 Digitizing Scope	$15,058	N2-9	B012741
01/15/92	HP	3335A Level Generator	$13,305	N2-10	2843A05511
03/01/92	SRS	DS345 Synth. Fnc. Gen	$2,401	N2-11	18725/1
03/04/92	General Kinetics	magnetic tape degausser	$2,436	N2-12	504-283D-3-0901
01/31/92	Fluke	Pulse Gen. PM5715/11	$1,995	N2-13	538349
01/31/92	Fluke	Pulse Gen. PM5715/11	$1,995	N2-14	538348
02/21/92	HP	35689 S-Parameter Set	$3,449	N2-15	3129A00145
02/20/92	Math Works	Matlab 386	$1,602	N2-16	36065
10/28/92	Math Works	Matlab upgrade	$304	N2-16	32675
10/14/92	Math Works	Signal process.toolbox	$295	L / V	367610
05/02/93	Math Works	Matlab/Windows upgrade	$250	L / V	
03/01/92	SRS	DS345 Synte. Fnc. Gen	$2,401	N2-17	18729/1
12/30/91	HP	DC pwr.sup. HP3610A	$300	L / V	3125K01055
12/30/91	HP	DC pwr.sup. HP3610A	$300	L / V	3125K01007
12/30/91	HP	DC pwr.sup. HP3611A	$300	L / V	3125K00577
12/30/91	HP	DC pwr.sup. HP3611A	$300	L / V	3125K00692
12/30/91	HP	DC pwr.sup. HP3611A	$300	L / V	3125K00847
12/30/91	HP	DC pwr.sup. HP3611A	$300	L / V	3125K00824
02/26/92	Ham Radio Outlet	Icom IC-726 Tranceiver	$1,070	N2-21	2582
02/26/92	Ham Radio Outlet	Heil BM-10-1 microphone / headset	$81	N2-21	none
02/26/92	Ham Radio Outlet	AT-150 Antenna Tuner	$376	N2-21	6928
02/26/92	Ham Radio Outlet	PS-55 Power Supply	$200	N2-21	14151
02/26/92	Henry's Radio	Cushcraft R7 Antenna	$370	N2-21	none
02/26/92	Ham Radio Outlet	Icom IC-726 Tranceiver	$1,070	N2-22	2757
02/26/92	Ham Radio Outlet	Heil BM-10-1 microphone / headset	$81	N2-22	none
02/26/92	Ham Radio Outlet	AT-150 Antenna Tuner	$376	N2-22	6684

Appendix A - HAARP Equipment Listing

Date	Vendor	Description	Cost	Tag	Serial Number
02/26/92	Ham Radio Outlet	PS-55 Power Supply	$200	N2-22	3184
02/26/92	Henry's Radio	Cushcraft R7 Antenna	$370	N2-22	none
02/26/92	Ham Radio Outlet	Icom IC-726 Tranceiver	$1,070	N2-23	2842
02/26/92	Ham Radio Outlet	Heil BM-10-1 microphone / headset	$81	N2-23	none
02/26/92	Ham Radio Outlet	AT-150 Antenna Tuner	$376	N2-23	7231
02/26/92	Ham Radio Outlet	PS-55 Power Supply	$200	N2-23	14243
02/26/92	Henry's Radio	Cushcraft R7 Antenna	$370	N2-23	none
03/17/92	Newark	Powerstat Variable Trans	$429	L / V	none
03/17/92	Newark	Powerstat Variable Trans	$429	L / V	none
12/17/91	IDS	ATI Modem E9600	$399	L / V	AT010353
12/18/91	PC CON	Iomega Transkit	$199	L / V	PP01480118
12/18/91	PC CON	90 MB Tripak	$439	L / V	none
04/28/92	Pasternack	Push Button Attenuator	$150	L / V	none
05/11/92	Pasternack	Push Button Attenuator	$150	L / V	none
05/11/92	Pasternack	Push Button Attenuator	$150	L / V	none
05/11/92	Pasternack	Push Button Attenuator	$150	L / V	none
05/11/92	Pasternack	Push Button Attenuator	$150	L / V	none
05/11/92	Pasternack	Push Button Attenuator	$150	L / V	none
02/07/92	Avnet Computer	ASPI DOS Manager	$60	L / V	none
10/14/92	Program. Shop	Watcom C 9.0/386	$614	L / V	none
10/14/92	Program. Shop	Pharlap 386 DOS DK	$450	L / V	none
02/04/92	NDPS	4 Mb Memory for HPLJ III	$270	L / V	none
02/11/92	NDPS	Printer Sharing Device	$360	L / V	10734
02/04/92	NDPS	Pacific Page Postscript	$345	L / V	15370
09/29/92	Cedar Comp.	HP Laserjet III 33449A	$1,425	N2-24	3220J02379
01/31/92	Piezo Crystal Co.	10 MHz time base	$650	N2-35	1
03/02/93	Kepco, Inc.	Power supply	$47	L/V	none
03/18/93	ITC Electronics	Power supply	$71	L/V	none
02/14/92	IDS	AMI MB,486-33	$2,200	N2-25	1620404330
04/22/93	Integrand Res.	Computer enclosures	$540	N2-25	none
02/13/92	Nat Inst	IEEE-488 Board	$495	N2-25	32352
02/13/92	Nat Inst	1m IEEE-488 Cable	$95	N2-25	none
02/14/92	IDS	AMI Host Bus Adapter	$795	N2-25	1512500664
02/13/92	Nat Inst	2m IEEE-488 Cable	$100	N2-25	none
02/13/92	Nat Inst	2m IEEE-488 Cable	$100	N2-25	none
04/27/93	IDS	Fujitsu Keyboard	$69	N2-25	none
05/25/93	Frys Electronics	Orchid Fahren. Video B.	$260	N2-25	FUR-11166
04/26/93	Frys Electronics	High Speed Ser. Port	$60	N2-25	none
04/26/93	Frys Electronics	Sony 1320 Monitor	$375	N2-25	7077355
04/26/93	Frys Electronics	Maxtor 7120 120 MB HD	$249	N2-25	MU2456324
04/26/93	Frys Electronics	Teac 5.25" Drive	$70	N2-25	none
04/26/93	Frys Electronics	Teac 3.5" Drive	$70	N2-25	none
04/26/93	Frys Electronics	DR-DOS 6.0	$60	N2-25	none

Appendix A - HAARP Equipment Listing

Date	Vendor	Description	Cost	Tag	Serial Number
04/26/93	Frys Electronics	DeskView Software	$140	N2-25	none
04/22/93	Integrand Res.	Computer enclosures	$540	N2-26	none
12/04/91	IDS	AMI Host Bus Adapter	$795	N2-26	1513401213
02/14/92	IDS	AMI MB,486-33	$2,200	N2-26	1614803114T
10/12/92	Ariel Corp.	DSP32C 16-bit digitizer	$3,840	N2-26	968
04/27/93	IDS	Fujitsu Keyboard	$69	N2-26	none
05/25/93	Frys Electronics	Orchid Fahren. Video B.	$260	N2-26	FUR-03947
04/26/93	Frys Electronics	Sony 1320 Monitor	$375	N2-26	7071421
04/26/93	Frys Electronics	Maxtor 7120 120 MB HD	$249	N2-26	MU2456865
04/26/93	Frys Electronics	Teac 5.25" Drive	$70	N2-26	none
04/26/93	Frys Electronics	Teac 3.5" Drive	$70	N2-26	none
04/26/93	Frys Electronics	DR-DOS 6.0	$60	N2-26	none
09/15/93	Genesis Engr.	Radar Controller	$7,277	N2-27	none
11/25/92	Genesis Engr.	Code Generator	$3,920	N2-28	none
10/14/92	LaSalle Res.	HF Receiver, RXHF-1	$15,000	N2-29	none
04/13/93	LaSalle Res.	50 MHz Radar Receiver	$10,000	N2-30	none
04/13/93	LaSalle Res.	50 MHz Radar Transmitter	$30,274	N2-31	none
12/15/93	LaSalle Res.	50 MHz Plasma Line Rec.	$15,000	N2-32	none
12/15/93	LaSalle Res.	28 MHz Radar Transmitter	$30,000	N2-33	none
12/15/93	LaSalle Res.	28 MHz Radar Receiver	$10,000	N2-34	none
Total discrete materials & hardware			$301,543		

Appendix A - HAARP Equipment Listing

Date	Vendor	Description	Cost	Tag	Serial Number
Tag #N2-18 is assigned to an 8-bit radar processor. The following is a list of key items that were used in the construction of radar processor N2-18.					
11/20/91	INTEG	Integrand Mother Case	$439	N2-18	505176
03/03/92	IDS	AMI Mark V 386/33 w 4Mb	$1,010	N2-18	4223513274
03/30/92	PC CON	Cyrix 83D87,33 MHz	$210	N2-18	none
02/28/92	Markenrich	Digitizing Card	$1,791	N2-18	128055 (8.1ns)
02/07/92	ICS	Counter/Timer Board	$296	N2-18	none
02/25/92	Analog Dev	RTI-860 A/D conv. ISA	$2,397	N2-18	128848
03/26/92	Optical Laser	Ten Time 4050 SCSI host	$272	N2-18	711011795
01/22/92	INTEG	Integrand Single Case	$174	N2-18	none
02/20/92	NDPS	Exabyte 8500s	$2,889	N2-18	2502726
01/22/92	INTEG	Integrand Single Case	$174	N2-18	none
02/07/92	SDI	Maxtor 680 MB Hard Drive	$1,459	N2-18	2A03104065
03/09/92	GRI	Radar Interface Box	$2,165	N2-18	4
12/24/91	IDS	Teac 1.2 Mb 5.25 Drive	$75	N2-18	4103604
12/24/91	IDS	Teac 1.44 Mb 3.5 Drive	$70	N2-18	K371825
12/04/91	IDS	ST1096N 80 MB HD	$389	N2-18	4C53542
12/04/91	IDS	Serial/Par. I/O card	$29	N2-18	none
02/04/92	PC Connection	90 MB Bernoulli	$799	N2-18	9411500344
12/04/91	IDS	Iomega PC2/B	$250	N2-18	5Q062F
12/18/91	IDS	Sony 1304 Monitor	$649	N2-18	5116799
12/20/91	CompUSA	Orchid ProDeignIIS VGA	$250	N2-18	61339
03/20/92	Avnet Computer	Adaptec SCSI host bus	$255	N2-18	B00661411
02/04/92	NDPS	DR DOS 6.0	$79	N2-18	none
03/30/92	NDPS	Novabac 3.5	$111	N2-18	10001
02/11/92	NDPS	Serial Mouse	$90	N2-18	60Q32 G
12/04/91	IDS	Fujitsu Key Board	$59	N2-18	6035501
03/04/92	ITT Pomona	Total Cabling Hardware	$585	L/V	none
03/04/92	ITT Pomona	Total Connect. Hardware	$339	L/V	none
12/19/91	ICS	Lithium Battery	$41	N2-18	none
Total materials cost for processor N2-18			$17,345		

Appendix A - HAARP Equipment Listing

Date	Vendor	Description	Cost	Tag	Serial Number
		Tag #N2-19 is assigned to an 8-bit radar processor. The following is a list of key items that were used in the construction of radar processor N2-19.			
01/22/92	INTEG	Integrand Mother Case	$439	N2-19	none
03/03/92	IDS	AMI Mark V 386/40 w 4Mb	$1,103	N2-19	S4220906412
03/30/92	PC CON	Cyrix 83D87,40 MHz	$210	N2-19	none
02/28/92	Markenrich	Digitizing Card	$1,791	N2-19	128054 (6.2ns)
02/07/92	ICS	Counter/Timer Board	$296	N2-19	none
02/25/92	Analog Dev	RTI-860 A/D conv. ISA	$2,397	N2-19	121675
03/30/92	Optical Laser	Ten Time 4050 SCSI host	$271	N2-19	711011678
02/02/92	Com.Auto&Cont	DSP32C w. 256k DRAM	$1,995	N2-19	1421
01/22/92	INTEG	Integrand Single Case	$174	N2-19	none
02/20/92	NDPS	Exabyte 8500s	$2,889	N2-19	2502689
01/22/92	INTEG	Integrand Single Case	$174	N2-19	none
02/04/92	NDPS	680 MB Maxtor Hard Drive	$1,532	N2-19	1L03104518
03/09/92	GRI	Radar Interface Box	$2,165	N2-19	0002
02/10/92	NDPS	Teac 1.2 Mb 5.25 Drive	$67	N2-19	K609838
02/10/92	NDPS	Teac 1.44 Mb 3.5 Drive	$62	N2-19	4224904
02/11/92	NDPS	Maxtor 80MB HD	$315	N2-19	4C53679
12/04/91	IDS	90 MB Bernoulli	$995	N2-19	9411490221
03/04/92	PC Conn	Iomega PC2/B	$250	N2-19	5Q062F
02/14/92	IDS	Serial/Par. I/O card	$29	N2-19	none
02/18/92	IDS	Sony 1304 Monitor	$649	N2-19	5107502
02/14/92	IDS	Orchid Pro II VGA , 1Mb	$249	N2-19	PROII252418
04/16/92	Avnet Computer	Adaptec SCSI host bus	$255	N2-19	B00937203
02/04/92	NDPS	DR DOS 6.0	$79	N2-18	none
03/30/92	NDPS	Novabac 3.5	$111	N2-19	10001
02/11/92	NDPS	Serial Mouse	$90	N2-19	PH620 X
02/14/91	IDS	Fujitsu Key Board	$59	N2-19	G9071441
03/04/92	ITT Pomona	Total Cabling Hardware	$585	L/V	none
03/04/92	ITT Pomona	Total Connect. Hardware	$339	L/V	none
03/30/92	IDS	Lithium Battery	$30	N2-19	none
01/22/93	Newark Electrn.	Heat sinks for MR board	$60	N2-19	none
	Total materials cost for processor N2-19		$19,660		

49

Appendix A - HAARP Equipment Listing

Date	Vendor	Description	Cost	Tag	Serial Number
Tag #N2-20 is assigned to an 8-bit radar processor. The following is a list of key items that were used in the construction of radar processor N2-20.
01/23/92	INTEG	Integrand Mother Case	$439	N2-20	none
03/25/92	IDS	AMI 386/33 w 4MB	$1,010	N2-20	S4220805398
12/18/91	PC CON	Cyrix 33/83D87 Chip	$195	N2-20	none
02/28/92	Markenrich	Digitizing Card	$1,791	N2-20	128057 (4.6ns)
02/07/92	ICS	Counter/Timer Board	$296	N2-20	none
02/25/92	Analog Dev	RTI-860 A/D conv. ISA	$2,397	N2-20	128841
03/30/92	Optical Laser	Ten Time 4050 SCSI host	$271	N2-20	711011675
11/20/91	INTEG	Integrand Double Case	$214	N2-20	none
12/04/91	IDS	Exabyte 8500s	$4,995	N2-20	2502609
02/07/92	SDI	680 MB Maxtor Hard Drive	$1,459	N2-20	2A03104062
03/09/92	GRI	Radar Interface Box	$2,165	N2-20	0003
02/10/92	NDPS	Teac 1.2 Mb 5.25 Drive	$67	N2-20	K481610
02/10/92	NDPS	Teac 1.44 Mb 3.5 Drive	$62	N2-20	4224905
02/11/92	NDPS	Maxtor 80MB HD	$315	N2-20	A409SFO5
02/04/92	PC Connection	90 MB Bernoulli	$799	N2-20	9412030561
03/04/92	PC Conn	Iomega PC2/B	$202	N2-20	5Q047H
02/18/92	IDS	Sony 1304 Monitor	$649	N2-20	5109052
02/14/92	IDS	Serial/Par. I/O card	$29	N2-20	none
02/14/92	IDS	Orchid Pro II VGA , 1Mb	$249	N2-20	830-0071-2 / B8
04/17/92	Avnet Computer	Adaptec SCSI host bus	$255	N2-20	B00931349
02/04/92	NDPS	DR DOS 6.0	$79	N2-20	none
03/30/92	NDPS	Novabac 3.5	$111	N2-20	10001
02/04/92	NDPS	Serial Mouse	$90	N2-20	6DQ37
02/14/92	IDS	Fujitsu Key Board	$59	N2-20	6035501
03/04/92	ITT Pomona	Total Cabling Hardware	$585	L/V	none
03/04/92	ITT Pomona	Total Connect. Hardware	$339	L/V	none
03/30/92	IDS	Lithium Battery	$30	N2-20	none
	Total materials cost for processor N2-20	$19,152		

Appendix A - HAARP Equipment Listing

Date	Vendor	Description	Cost	Tag	Serial Number
03/30/92	Masco Elect.	Shipping containers AL2825-1605	$470	L / V	none
03/30/92	Masco Elect.	Shipping containers AL2825-1605	$470	L / V	none
03/30/92	Masco Elect.	Shipping containers AL2825-1605	$470	L / V	none
03/30/92	Masco Elect.	Shipping containers AL2825-1605	$470	L / V	none
03/30/92	Masco Elect.	Shipping containers AL2825-1605	$470	L / V	none
03/30/92	Masco Elect.	Shipping containers AL2825-1605	$470	L / V	none
03/30/92	Masco Elect.	Shipping containers AL2825-1605	$470	L / V	none
03/30/92	Masco Elect.	Shipping containers AL2825-1605	$470	L / V	none
03/30/92	Masco Elect.	Shipping containers AL2825-1605	$470	L / V	none
03/30/92	Masco Elect.	Shipping containers AL2825-1605	$470	L / V	none
03/30/92	Masco Elect.	Shipping containers AL2825-1605	$470	L / V	none
03/30/92	Masco Elect.	Shipping containers AL2825-1605	$470	L / V	none
03/30/92	Masco Elect.	Shipping containers AL2825-1605	$470	L / V	none
03/30/92	Masco Elect.	Shipping containers AL2221-1205	$386	L / V	none
03/30/92	Masco Elect.	Shipping containers AL2221-1205	$386	L / V	none
03/30/92	Masco Elect.	Shipping containers AL2221-1205	$386	L / V	none
Total materials cost for shipping containers			$7,268		
Grand total for materials & hardware purchased under NAS8-39238			$364,968		